

Limits on the Macho Content of the Galactic Halo from the EROS-2 Survey of the Magellanic Clouds^{*}

P. Tisserand^{1**}, L. Le Guillou^{1***}, C. Afonso^{1†}, J.N. Albert², J. Andersen⁵, R. Ansari², É. Aubourg^{1‡}, P. Bareyre¹, J.P. Beaulieu³, X. Charlot¹, C. Coutures^{1,3}, R. Ferlet³, P. Fouqué^{7,8}, J.F. Glicenstein¹, B. Goldman^{1§}, A. Gould⁶, D. Graff^{6¶}, M. Gros¹, J. Haissinski², C. Hamadache¹, J. de Kat¹, T. Lasserre¹, É. Lesquoy^{1,3}, C. Loup³, C. Magneville¹, J.B. Marquette³, É. Maurice⁴, A. Maury^{8||}, A. Milsztajn¹, M. Moniez², N. Palanque-Delabrouille¹, O. Perdureau², Y.R. Rahal², J. Rich¹, M. Spiro¹, A. Vidal-Madjar³, L. Vigroux^{1,3}, S. Zylberajch¹
The EROS-2 collaboration

¹ CEA, DSM, DAPNIA, Centre d'Études de Saclay, F-91191 Gif-sur-Yvette Cedex, France

² Laboratoire de l'Accélérateur Linéaire, IN2P3 CNRS, Université de Paris-Sud, F-91405 Orsay Cedex, France

³ Institut d'Astrophysique de Paris, UMR 7095 CNRS, Université Pierre & Marie Curie, 98 bis Boulevard Arago, F-75014 Paris, France

⁴ Observatoire de Marseille, 2 place Le Verrier, F-13248 Marseille Cedex 04, France

⁵ The Niels Bohr Institute, Copenhagen University, Juliane Maries Vej 30, DK-2100 Copenhagen, Denmark

⁶ Department of Astronomy, Ohio State University, Columbus, OH 43210, U.S.A.

⁷ Observatoire Midi-Pyrénées, Laboratoire d'Astrophysique (UMR 5572), 14 av. E. Belin, F-31400 Toulouse, France

⁸ European Southern Observatory (ESO), Casilla 19001, Santiago 19, Chile

Received;accepted

ABSTRACT

Aims. The EROS-2 project was designed to test the hypothesis that massive compact halo objects (the so-called “machos”) could be a major component of the dark matter halo of the Milky Way galaxy. To this end, EROS-2 monitored over 6.7 years 33×10^6 stars in the Magellanic clouds for microlensing events caused by such objects.

Methods. In this work, we use only a subsample of 7×10^6 bright stars spread over 84 deg^2 of the LMC and 9 deg^2 of the SMC. The strategy of using only bright stars helps to discriminate against background events due to variable stars and allows a simple determination of the effects of source confusion (blending). The use of a large solid angle makes the survey relatively insensitive to effects that could make the optical depth strongly direction dependent.

Results. Using this sample of bright stars, only one candidate event was found, whereas ~ 39 events would have been expected if the Halo were entirely populated by objects of mass $M \sim 0.4M_\odot$. Combined with the results of EROS-1, this implies that the optical depth toward the Large Magellanic Cloud (LMC) due to such lenses is $\tau < 0.36 \times 10^{-7}$ (95% CL), corresponding to a fraction of the halo mass of less than 8%. This optical depth is considerably less than that measured by the MACHO collaboration in the central region of the LMC. More generally, machos in the mass range $0.6 \times 10^{-7}M_\odot < M < 15M_\odot$ are ruled out as the primary occupants of the Milky Way Halo.

Key words. Galaxy:halo - Cosmology: dark matter - Gravitational Lensing

1. Introduction

Since the proposal (Paczynski 1986; Petrou 1981) that dark matter in the form of faint compact objects (machos¹) could be found through gravitational microlensing, the EROS, MACHO, OGLE, MOA and SuperMACHO collaborations have monitored millions of stars in the Magellanic Clouds to search for microlensing events. Such events would be due to a lensing object passing near the line of sight toward a background Magellanic star, causing a transient magnification of the star's primary image as well as creating a secondary image. Neither the image separation nor the image size are normally resolvable, so the only easily observable effect during an event is an apparent transient amplification of the star's flux. The amplification is greater than a factor 1.34 if the line of sight to the star passes within the lens's Einstein ring of squared radius $r_E^2 = 4GMD_s x(1-x)/c^2$

¹ for “Massive Astrophysical Compact Halo Objects” (Griest 1991), not to be confused with the “MACHO collaboration.”

^{*} Based on observations made with the Marly telescope at the European Southern Observatory, La Silla, Chile.

^{**} Now at Research School of Astronomy and Astrophysics, Australian National University, Mount Stromlo Obs., Cotter Rd., Weston, ACT 2611, Australia

^{***} now at LPNHE, CNRS-IN2P3 and Universités Paris 6 et Paris 7, 4 Place Jussieu, F-75252 Paris Cedex 05 France

[†] Now at Max-Planck-Institut für Astronomie, Königstuhl 17, D-69117 Heidelberg, Germany

[‡] Also at APC, 10, rue Alice Domon et Lonie Duquet, F-75205 Paris Cedex 13, France

[§] Now at Max-Planck-Institut für Astronomie, Königstuhl 17, D-69117 Heidelberg, Germany

[¶] Now at Division of Medical Imaging Physics, Johns Hopkins University Baltimore, MD 21287-0859, USA

^{||} Now at San Pedro de Atacama Celestial Exploration, Casilla 21, San Pedro de Atacama, Chile

where D_s is the distance to the star and $x D_s$ is the distance to the lens of mass M . The optical depth for microlensing, i.e. the probability that at a given time a given star is amplified by more than a factor 1.34, is

$$\tau = \frac{4\pi G D_s^2}{c^2} \int_0^1 dx \rho(x) x(1-x), \quad (1)$$

where ρ is the mass density of lenses. For source stars in the Magellanic Clouds, the order of magnitude of τ is $f v_{\text{rot}}^2 / c^2 \sim f \times 10^{-6}$ where $v_{\text{rot}} \sim 220 \text{ km s}^{-1}$ is the rotation velocity of the Milky Way and f is the fraction of the halo mass that is comprised of lensing objects. The factor of proportionality between τ and $f v_{\text{rot}}^2 / c^2$ depends on the structure of the Halo. The benchmark value is often taken to be that for a spherical isothermal halo of core radius 5 kpc, the so-called ‘‘S model’’ used by the MACHO collaboration (Alcock et al. 2000b; Griest 1991). For the Large Magellanic Cloud (LMC) this gives

$$\tau_{\text{lmc}} = 4.7 f \times 10^{-7}. \quad (2)$$

For the Small Magellanic Cloud (SMC), the S model gives $\tau_{\text{smc}} \sim 1.4 \tau_{\text{lmc}}$. For a flattened halo, one finds a smaller value, typically $\tau_{\text{smc}} \sim \tau_{\text{lmc}}$ (Sackett and Gould 1993).

Magellanic stars can also be lensed by non-halo stars, either in the Magellanic Clouds or in the Milky Way disk. Lensing by disk stars is expected to have an optical depth of order 10^{-8} (Alcock et al. 2000b). The optical depth for lensing by ‘‘self-lensing’’, i.e. lensing by stars in the Clouds, is expected to range from $\sim 5 \times 10^{-8}$ in the center of the LMC bar to $\sim 0.5 \times 10^{-8}$ at 3 deg from the bar (Mancini et al. 2004). For the SMC, the self-lensing optical depth is expected to be somewhat larger, $\sim 4 \times 10^{-8}$ averaged over the central 10 deg^2 (Graff & Gardiner 1999).

Microlensing events are characterized by a timescale t_E giving the time for the lens to travel a distance corresponding to its Einstein radius, $t_E = r_E / v_t$ where v_t is the lens’s transverse velocity relative to the line of sight. For high amplification events, $2t_E$ is the time over which the amplification is $A > 1.34$. Since r_E is proportional to the square root of the lens mass M , the mean t_E will scale like $M^{1/2}$. The S model has a 3-dimensional macho velocity dispersion of 270 km s^{-1} and gives

$$\langle t_E \rangle \sim 70 \left(\frac{M}{M_\odot} \right)^{1/2} \text{ days}. \quad (3)$$

Much excitement was generated by the MACHO collaboration’s measurement of the LMC microlensing rate which suggested that a significant amount of the Milky Way’s Halo is comprised of machos. Their latest analysis (Alcock et al. 2000b) used 13/17 observed events² to measure an optical depth of $\tau_{\text{lmc}} / 10^{-7} = 1.2^{+0.4}_{-0.3}$ (*stat*) with an additional 20% to 30% systematic error. This would correspond to a Halo fraction $0.08 < f < 0.50$ (95% CL). The mean t_E of their events was 40 d corresponding to machos in the mass range $0.15 M_\odot < M < 0.9 M_\odot$. On the other hand the EROS collaboration (Lasserre et al. 2000; Afonso et al. 2003a) has placed only an upper limit on the halo fraction, $f < 0.2$ (95% CL) for objects in this mass range, ruling out a large part of the range of f favored by the MACHO collaboration.

Bennett (2005) argued that the MACHO optical depth should be reduced to $\tau_{\text{lmc}} / 10^{-7} = 1.0 \pm 0.3$ in order to take into account

² 13 of the 17 events satisfied their so-called A criteria intended to identify high signal-to-noise events. The other 4 events, so-called B events, are selected by looser cuts.

contamination by variable stars. This paper made use of the observation by the EROS collaboration (Tisserand 2004) of further variability of one of the MACHO A candidates, indicating intrinsic stellar variability. The paper also noted that the spectrum of the MACHO B candidate MACHO-LMC-22 indicated that the source is an active background galaxy, as reported in Alcock et al. (2001b) where the event was eliminated from the sample for studying high-mass lenses. Using four MACHO A candidates whose microlensing nature was confirmed by precision photometry and the one A candidate rejected as a variable star, Bennett (2005) performed a likelihood analysis to argue that 11 ± 1 of the 13 A candidates are likely to be microlensing events, yielding the revised optical depth.

Machos can also be searched for by monitoring M31 and looking for temporal variations of surface brightness consistent with a star in M31 being microlensed. Candidate events have been reported by the VATT (Uglesich et al. 2004), WeCAPP (Riffeser et al. 2003), POINT-AGAPE (Calchi Novati et al. 2005), MEGA (de Jong et al. 2006) and Nainital (Joshi et al. 2005) collaborations. The POINT-AGAPE and MEGA collaborations presented efficiency calculations allowing them to constrain the content of the M31 and Milky Way halos. The disagreement between these two collaborations parallels that between the MACHO and EROS collaborations with the AGAPE collaboration finding a halo fraction in the range $0.2 < f < 0.9$, while the MEGA collaboration finds a halo fraction $f < 0.3$.

In this paper, we extend our previous analysis to find $\tau_{\text{lmc}} < 0.36 \times 10^{-7}$ (95% CL) for $M \sim 0.4 M_\odot$, corresponding to $f < 0.08$. Unlike the previous EROS limit, this is significantly lower than the optical depth measured by the MACHO collaboration. Unlike all previous analyses, we use only a bright, well-measured subsample of the Magellanic stars, about 20% of the total. We believe that the use of this bright subsample gives more reliable limits on the optical depth than measurements using faint stars. There are two reasons for this. First, bright stars have well reconstructed light curves that permit discrimination of intrinsically variable stars. Second, the use of bright stars makes it relatively simple to estimate so-called blending effects where reconstructed fluxes can receive contributions from more than one star, complicating the interpretation of events.

EROS-2 is a second generation microlensing experiment. The first generation, EROS-1, consisted of two programs, both at the European Southern Observatory (ESO) at La Silla, Chile. The first program (Ansari et al. 1996a) used Schmidt photographic plates to monitor a 27 deg^2 region containing the LMC bar during the southern summer from October, 1990 through April, 1993. With a sampling frequency of up to one image per night, it was sensitive mostly to machos in the range $10^{-4} M_\odot < M < 1 M_\odot$. The second program (Renault et al. 1998) used a 0.4 deg^2 CCD mosaic from December 1991 through March, 1995 to monitor one field in the LMC bar and another in the SMC. With up to 40 images taken per night, this program was sensitive mostly to machos in the range $10^{-7} M_\odot < M < 10^{-3} M_\odot$. The results of these two EROS-1 programs are summarized in Renault et al. (1997).

The second generation program described here, EROS-2, used the Marly 1 meter telescope at ESO, La Silla. The telescope was equipped with two 0.95 deg^2 CCD mosaics to monitor 93 deg^2 in the Magellanic Clouds, 63 deg^2 in the Galactic Bulge, and 28 deg^2 in the spiral arms of the Milky Way. The observations were performed between July 1996 and February 2003 (JD between 2,450,300 and 2,452,700).

Besides the Magellanic results presented here, EROS-2 has also published measurements of the optical depth toward the Galactic Bulge (Afonso et al. 2003b; Hamadache et al. 2006). The measured optical depth is in agreement with that measured by MACHO (Popowski et al. 2005), and OGLE-2 (Sumi et al. 2006) and with the predictions of Galactic models (Evans & Belokurov 2002; Bissantz & Gerhard 2002; Han & Gould 2003; Wood and Mao 2005).

EROS-1 and EROS-2 overlapped with the MACHO program that monitored $\sim 13.4 \text{ deg}^2$ of the LMC from July, 1992 through January, 2000. Three other wide-angle microlensing searches are now in operation: MOA³ (since August, 1998), OGLE-3⁴ (since June, 2001) and SuperMACHO⁵ (since October, 2001).

In this article, we report on the analysis of the full EROS-2 data set (July 1996 till February 2003) toward the Magellanic Clouds. Our previous analyses reported on 5 years of data and 5 million stars toward the SMC (Afonso et al. 2003a), and 2 years of data and 17 million stars toward the LMC (Lasserre et al. 2000). An update of the LMC analysis was reported in Milsztajn et al. (2001) and Lasserre (2000), which dealt with 25 million stars and 3 years. The limits determined in the previous analyses are refined in the analysis presented here. More details about the present analysis can be found in Tisserand (2004).

The plan of the article is as follows. In Section 2, we recall the basics of the EROS-2 setup, give the general characteristics of the data sample and describe the data reduction steps used to produce the light curves. Section 3 presents the Bright-Star Sample of stars to be used in the measurement of the optical depth. In Section 4, we describe the selection criteria used to choose the microlensing candidates in the Bright-Star Sample. (Selection of events in the full sample is described in Appendix A.) Section 5 presents the final sample of selected events from the Bright-Star Sample as well as events found by relaxing the selection criteria. In Section 6 we discuss the status of former EROS-1 and EROS-2 microlensing candidates as well as those of the MACHO collaboration. In Section 7, we describe the computation of the EROS-2 detection efficiency. Section 8 presents the limit on the optical depth and on the abundance of machos in the Galactic halo by combining all EROS-1 and EROS-2 data. We conclude in Section 9 with a discussion of the significance of the limit, and a comparison with the results of Alcock et al. (2000b).

2. Experimental setup, observations and data reduction

The EROS-2 Marly telescope, camera, telescope operations and data reduction are described in Bauer et al. (1997), Palanque-Delabrouille et al. (1998), and references therein. Here we give only general information, and details or modifications that are specific to the present analysis.

2.1. The setup and the data

The Marly telescope is a one meter diameter Ritchey-Chrétien ($f = 5.14\text{m}$), equipped with two wide angle CCD cameras. Each camera is a mosaic of 8 CCDs, 2 along right ascension and 4 along declination. Each CCD has 2048×2048 pixels of $15 \times 15 \mu\text{m}^2$ size, corresponding to $0.602 \times 0.602 \text{ arcsec}^2$.

³ <http://www.phys.canterbury.ac.nz/moa/>

⁴ <http://bulge.astro.princeton.edu/~ogle/>

⁵ <http://www.ctio.noao.edu/~supermacho/>

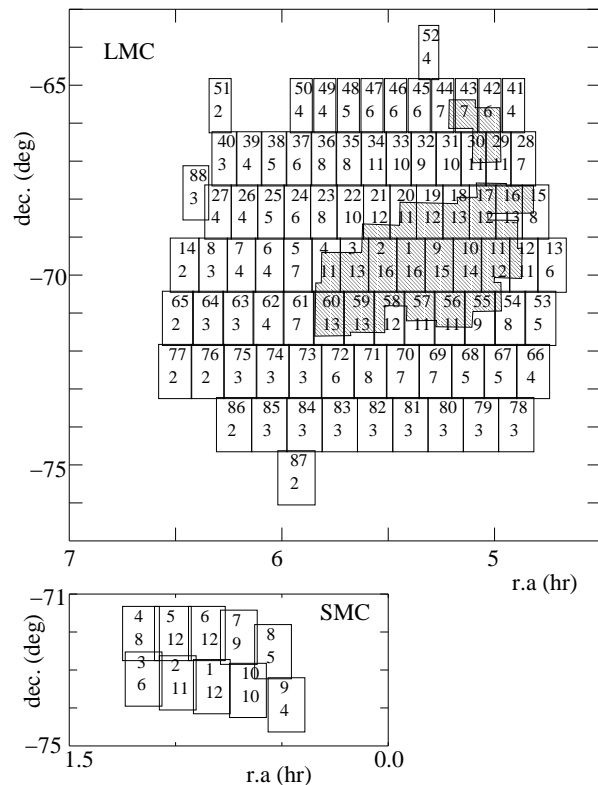


Fig. 1. Map of the EROS-2 LMC and SMC fields in equatorial coordinates. A total of 88 LMC and 10 SMC fields were monitored. The first number in each field is the field number and the second is the number of bright stars (as defined in Section 3) in the field in units of 10^4 . The two shaded regions (the larger one centered on the LMC bar) are the 13.4 deg^2 used by the MACHO collaboration to measure the optical depth (Alcock et al. 2000b).

Images were taken simultaneously in two wide passbands, so-called R_{eros} centered close to the I_C standard band, and B_{eros} intermediate between the standard V and R bands. While no results presented here depend on the photometric calibration, almost all of our fields could be calibrated using stars from the catalogs of the Magellanic Clouds Photometric Survey (Zaritsky et al. 2004). For 4.5 deg^2 , the calibration was checked with the OGLE-II catalog (Udalski et al. 2000b). To a precision of $\sim 0.1 \text{ mag}$, the EROS magnitudes satisfy

$$R_{\text{eros}} = I_C \quad B_{\text{eros}} = V_J - 0.4(V_J - I_C). \quad (4)$$

The observed fields correspond to 0.95 deg^2 each and they are twice as large in declination than in right ascension ($1.38 \times 0.69 \text{ deg}^2$). A total of 88 fields have been monitored toward the LMC and 10 toward the SMC. The positions of the fields are shown in Figure 1. The exposure times ranged from 180 s to 900 s. The fields have been sampled differently, according to their stellar density and distance from the optical centers of the LMC and the SMC. Broadly, there are three families of LMC fields : in the first 3 years of operation, 22 outer fields were seldom imaged, 22 fields were imaged about 100 times and the remaining 44 inner fields were imaged over 200 times. Later, from July 1999 on, all 88 LMC fields were imaged with a similar sampling. The number of photometric measurements, per star and per band, ranges from 300 to 600 in the LMC fields.

The ten SMC fields were imaged with a similar sampling, except in 2001 and 2002 when the inner six fields were imaged twice as often as the four outer ones. The number of photometric

measurements, per star and per band, ranges from 600 to 900 in these SMC fields.

After rejection of bad images (11%) due to bad seeing, high sky background or instrumental problems, the average numbers of measurements used in the analysis, per star and per band, are about 430 and 780 in the LMC and SMC fields respectively.

2.2. Template Images

The production of light curves proceeded in three steps : template image construction, star catalog production from the templates, and photometry of individual images to obtain the light curves.

The template images were obtained by co-adding 15 images of each field; they were resampled so that the templates have twice as many pixels as the original images. The 15 images were chosen among the best ones available, i.e. with low sky background, good seeing, and with a large number of stars (as estimated from a quick first look algorithm). All images susceptible to enter the template construction were checked for the absence of long tracks, caused by satellites, planes or meteors. For technical reasons linked to computing and to PSF variation within one CCD, the CCD images were divided in four quadrants, such that there were in total 6272 template images (98 fields, 8 CCDs, 4 quadrants, 2 passbands). In order to ensure relatively uniform zeropoints of the 6272 templates, we required that the first image used in template construction (to which the other 14 images were photometrically aligned) be registered within a short time interval with good and uniform sky conditions (23rd to 26th, November 2000). For each field, the same epochs were used in the construction of the templates in the two passbands.

The stars were identified on the template images using a pseudo-image that we call a correlation image. Each pixel of this image contains the correlation coefficient of neighboring pixels of the template itself with a two-dimensional Gaussian PSF. Each group of pixels satisfying some threshold value on the pseudo-image was retained as a star in the catalog. In previous EROS-2 analyses, the thresholds were identical for all templates; this had led to over 20% failures in this cataloging step. The present analysis has chosen to progressively relax the thresholds when such failures occur; in this way, the cataloging step failures were drastically reduced. (The number of identified stars on fields using relaxed thresholds was lower on average.) The star catalogs obtained from the template images in the two passbands were then merged. A star was retained only if it was detected in both. The overall efficiency of the template plus star catalog construction was excellent; only 24 CCD quadrants could not be processed out of a total of 3136.

Examples of color-magnitude diagrams can be found in Figures 7 to 10 and A.1 to A.5. They are all characterized by a prominent group of clump giants and a main sequence whose relative strength varies from field to field. There are also stars that are redder than Magellanic red giants. Most of them are likely to be foreground stars in the disk of the Milky Way and their number is consistent with the predictions of Galactic models (Robin et al. 2003).

2.3. Light Curves

Photometry was then performed on each image of a given quadrant in turn with software specifically designed for crowded fields, PEIDA (Photométrie et Étude d’Images Destinées à l’Astrophysique) (Ansari et al. 1996b). First, the image was geo-

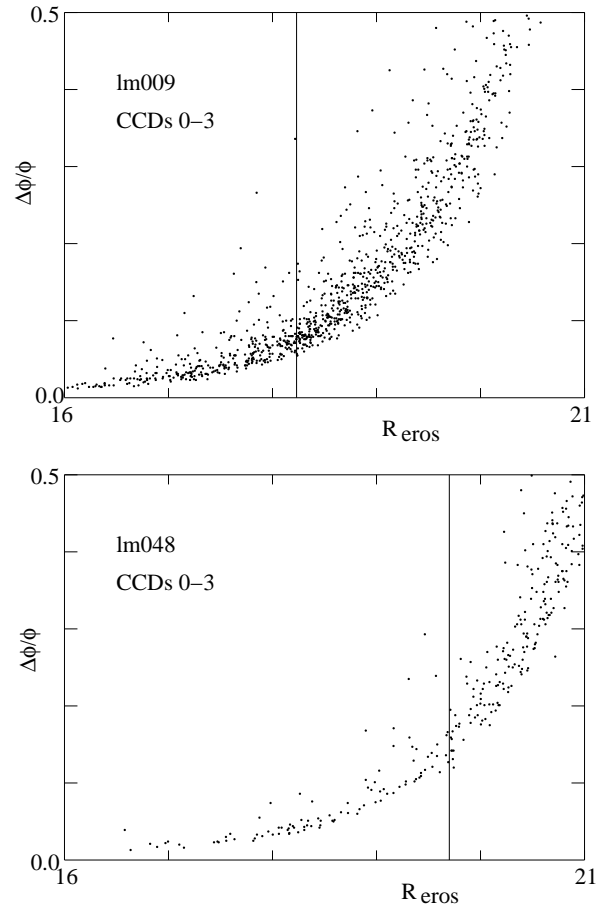


Fig. 2. The photometric precision as a function of R_{eros} for the dense field Im009 (top) and the sparse field Im048 (bottom). Each point represents the r.m.s. dispersion of the measurements for a single star after elimination of outliers. The vertical line shows the position of the bright-star magnitude cut (5) for the field, $R_{\text{eros}} = 18.23$ for Im009 CCDs 0-3 and $R_{\text{eros}} = 19.7$ for Im048 CCDs 0-3.

metrically aligned with the template. Then, imposing the star position determined from the template image, PSF-fitting photometry was performed for all stars by a linear least-squares method involving the star and all neighbors closer than 11 pixels, plus a sky background. An estimate of the error on this flux measurement was computed that depends on the photon statistics and on the overall quality of the photometered image. Typical photometric precisions are shown in Figure 2.

Before the analysis was started, we removed from the light curves measurements taken under far from normal conditions. This happened not infrequently, as the data taking policy was to work whenever possible, leaving to the analysis the task of rejecting these abnormal measurements. These were identified by extreme values of the sky background, seeing or absorption. In addition, images where the photometry failed for over 40% of cataloged stars were eliminated, as well as images for which more than 12% of the stars showed an excursion from their average flux larger than three standard deviations. Depending on the CCD, the number of rejected images varied between 7 and 18%, with an average of 11%.⁶

⁶ The largest single cause for rejection was the malfunction that affected 5 CCDs of the R_{eros} passband camera starting in January 2002.

To reduce systematic errors in the photometry, each light curve was searched for significant linear correlations between the measured flux and three observational variables, the seeing, the hour angle and the airmass. This was done independently in the two passbands. The measured fluxes were corrected linearly by requiring a vanishing correlation coefficient between the corrected fluxes and the given variable. The largest correlation was found with the seeing, in both passbands. For the bright stars considered in this work, the correction has only a small influence on the point-to-point dispersion of the lightcurves, reducing it on average by 6%.

A potential problem with this correction is that an artificial correlation can be induced if a real flux variation happens to occur during a period of poor seeing (for example). In this case, application of the correction would reduce the amplitude of the real flux variation but increase the point-to-point dispersion of the curve by making an incorrect flux correction. To guard against this possibility, we did not apply the correction if it increases the point-to-point dispersion of the light curves.

2.4. The Full Sample of Stars

A total of 58.4 million objects were found on the template images of both passbands – 51.8 million in the LMC and 6.6 million in the SMC. We chose to ignore those stars for which the association between the objects detected separately in the two passbands was doubtful or ambiguous (8.4 million) and objects that are dimmer than about twice the typical size of sky background fluctuations (14.9 million). We rejected light curves for which more than half of the photometry points are absent (1.0 million). Finally, we did not consider stars whose photometry is unstable due to its environment. This includes stars close to a very bright field star ($V_j < 10.1$, probably in the Galactic disk) and stars close to a visible diffraction feature in the PSF of bright stars; these two categories contain respectively 1.1% and 0.8% of the remaining stars.

We removed from consideration stars in field Im003, CCD0 which has numerous events caused by light echos from SN1987a. The echos generate arc-like images that appear to move a few arcsec per year⁷, causing false variations of a star's flux as the arc passes through the star's position.

After these cuts, 33.4 million objects remained, 29.2 million in the LMC and 4.2 million in the SMC. This constitutes the Full Sample of EROS-2 stars. In the next section we describe the selection of the Bright-Star Sample used for the measurement of optical depths.

3. The Bright-Star Sample

We have chosen to restrict our analysis to the Bright Sample of stars defined below. Besides the obvious advantage of ensuring a good photometric resolution, we do this to simplify the evaluation of the number of expected events predicted by a model. In crowded fields, this evaluation is complicated by “blending”, i.e. the fact that photometry of a given *object* can be influenced by more than one *star*. We shall see that these effects are rather small and simple to evaluate for the Bright-Star Sample (which should, strictly speaking, be called the Bright-Object Sample).

We have thus chosen to reject all measurements taken in 2002 and 2003 for these 5 CCDs.

⁷ Using 1000 pictures of this region co-added by groups of 10, we have produced a film that shows the motion of the light echos; it can be found at the URL <http://eros.in2p3.fr/EchoesSN1987a/>

Limiting the number of studied objects limits the sensitivity of the experiment so the magnitude cut must be a compromise between quantity and quality of objects. The efficiency calculations of Section 7 for unblended sources indicated that keeping only the $\sim 20\%$ brightest stars reduces by only $\sim 50\%$ the number of simulated microlensing events that pass our selection criteria. We therefore initially decided to accept a nominal $\sim 50\%$ loss of events by requiring $R_{\text{eros}} < R_{\text{median}}$, where R_{median} is the median R_{eros} for simulated unblended microlensing events passing our event selection criteria. R_{median} ranges from ~ 18.2 in the densest fields to ~ 20.5 in the sparsest. However, for sparse fields far from the LMC bar, in order to have a reasonable object reconstruction efficiency, a stricter cut was found to be necessary, $R_{\text{eros}} < 19.7$.

The final sample of bright stars is therefore defined by

$$16.0 < R_{\text{eros}} < R_{\text{max}} \quad R_{\text{max}} = \min(R_{\text{median}}, 19.7) . \quad (5)$$

The minimum magnitude $R_{\text{eros}} = 16$ was chosen to avoid the large number of variable stars brighter than this.

The position of the magnitudes cut are shown in the color-magnitude diagrams of Figures 7 to 10 and A.1 to A.5. Generally speaking, the cut includes clump giants but not the numerous main sequence stars seen far below the clump. Other than the small number of bright main sequence stars, we therefore employ stars of colors and magnitudes similar to those used in Galactic Bulge measurements that use clump giants (Hamadache et al. 2006).

It turns out that the cut (5) gives a rather uniform photometric precision for the Bright-Star Sample. Figure 3 shows the distribution of precision with a mean in both bands of $\sim 7\%$. The precision in dense fields hardly differs from that in sparse fields and the precision in the LMC hardly differs from that in the SMC.

The number of EROS-2 objects in the Bright-Star Sample defined by (5) is 6.05 million in the LMC and 0.90 million in the SMC. We must subtract from these numbers the expected number of foreground stars in the Milky Way disk. The Besançon model of the Milky Way (Robin et al. 2003) predicts that 0.56 million (LMC) and 0.04 million (SMC) are foreground Milky Way stars, consistent with the number of stars we observe that are redder than Magellanic red giants. The number of Bright-Sample stars to be used for optical depth measurements must therefore be reduced by 9% (4%) for the LMC (SMC), giving

$$N_{\text{objects}} = 5.49 \times 10^6 \quad (\text{LMC}) ; \quad (6)$$

$$N_{\text{objects}} = 0.86 \times 10^6 \quad (\text{SMC}) . \quad (7)$$

We now show how we evaluate the effect of blending on the Bright-Star Sample. For a given lens model (defined by the spatial, velocity and mass distribution of lenses), the expected number of detected events is

$$N_{\text{ex}} = \frac{2}{\pi} \frac{T_{\text{obs}}}{\langle t_E \rangle} \tau \sum_{i=1}^{N_{\text{stars}}} \langle \epsilon_i \rangle \quad (8)$$

where T_{obs} is the observing period, $\langle t_E \rangle$ is the mean Einstein radius crossing time given by the model, e.g. (3), and τ is the optical depth. The sum is over all observed stars and the “efficiency”, $\langle \epsilon_i \rangle$, is the expected ratio between the number of events passing the selection cuts of Section 4 and the number of events with $u < 1$ occurring during the observation period. The efficiency must be averaged over the t_E distribution given by the model.

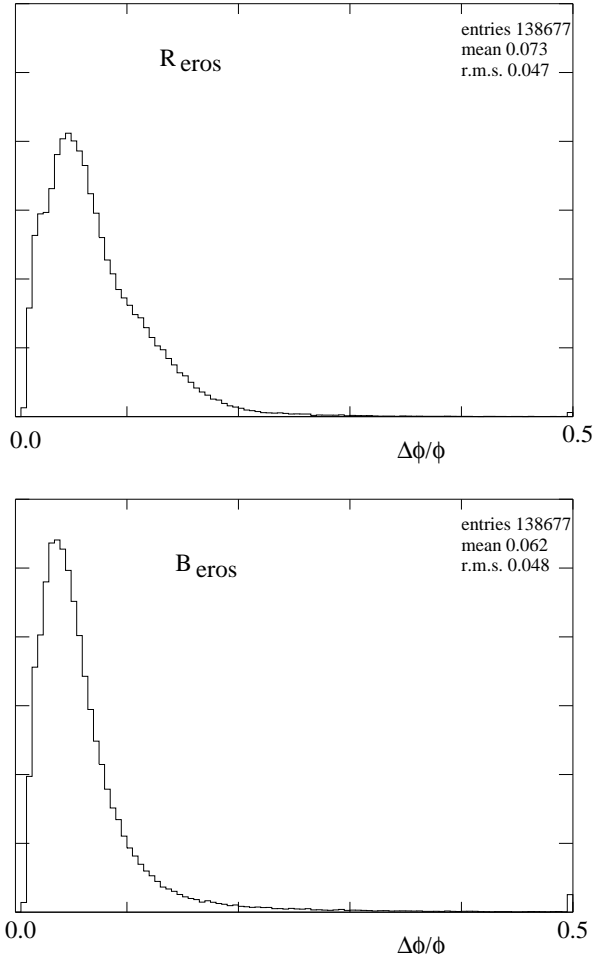


Fig. 3. The flux precision, $\Delta\phi/\phi$, for the Bright-Star Sample (2% of the sample are in the histograms). Each entry is the mean flux uncertainty for a star on its light curve. The top (bottom) histograms are for the R_{eros} (B_{eros}) bands.

EROS photometry is performed on a set of “objects” found on a reference image. In crowded fields, the correspondence between objects and stars is not straightforward. Generally speaking, most objects are dominated by one star, i.e. by the brightest star in the object’s seeing disk. However, if a fainter star in the seeing disk is microlensed, EROS photometry will assign some of the extra flux to the object with the remainder assigned to sky background. It is thus convenient to rewrite (8) as

$$N_{\text{ex}} = \frac{2}{\pi} \frac{T_{\text{obs}}}{\langle t_E \rangle} \tau \sum_{j=1}^{N_{\text{objects}}} \sum_i \langle \epsilon_{ij} \rangle \quad (9)$$

where the second sum is over the stars i near the object j . The efficiency, $\langle \epsilon_{ij} \rangle$, is again the expected ratio (averaged over t_E) between the number of microlensings of star i that pass selection cuts and the number of microlensings of star i with $u < 1$ occurring during the observation period. Since we do not know the stars in the seeing disk of each object, we must estimate the sum statistically using knowledge of the luminosity function. We will see that sum is dominated by the brightest star, $i = 1$, with contributions from the second brightest, $i = 2$, of order 10%.

If there were no blending, the efficiency could be estimated by modifying a sample of light curves with measured fluxes $F_0(t)$ by

$$F(t) = F_0(t) \frac{u^2 + 2}{u \sqrt{u^2 + 4}}, \quad u(t)^2 = u_0^2 + [(t - t_0)/t_E]^2, \quad (10)$$

where $u(t)$ is the distance of the lens to the star’s line-of-sight in units of the Einstein radius, u_0 is this distance at the time, t_0 , of maximum amplification, and t_E is the Einstein ring radius crossing time. The modified lightcurves can then be subjected to the selection criteria and the efficiency deduced by averaging over t_E and u_0 .

For blended events only a fraction α of an object’s flux is amplified. If the fraction is independent of amplification, the resulting light curve is

$$F(t) = F_0(t) \left[(1 - \alpha) + \alpha \frac{u^2 + 2}{u \sqrt{u^2 + 4}} \right]. \quad (11)$$

The efficiency to see such events now depends on α : $\epsilon_{ij} = \epsilon_{ij}(\alpha_i)$. Stars with small α_i require a small impact parameter u_0 to give a sufficiently large reconstructed amplification. Since our selection criteria require a reconstructed amplification greater than 1.34 ($u_0 = 1$ for $\alpha = 1$), the primary effect of blending is to reduce the efficiency by a factor $u_i(\alpha_i)$, the impact parameter needed for star i to produce a reconstructed amplification of 1.34. The efficiency is reduced by this factor because of the flat a priori u distribution. Additionally, the event appears shorter by a factor u_i further modifying the efficiency.

A simple example is two superimposed stars of the same magnitude and color. In this case $\alpha_1 = \alpha_2 = 0.5$ and $u_1 = u_2 \sim 0.7$. Before efficiency corrections, the event rate would be $0.7 + 0.7 = 1.4$ times the rate calculated ignoring blending. If the two stars have colors differing by $\Delta(B - R)_{\text{eros}} = 0.7$, the requirement that $A_{\text{max}} > 1.34$ in both colors yields a rate that is increased by a factor 1.3 over the rate for $\alpha = 1$.

To statistically evaluate the distribution of the α_i for Bright-Sample objects, a spectrum of 8000 artificial stars was placed at random positions on real EROS images (lm009, lm019, lm034, lm048) to give artificial images (xm009, xm019, xm034, xm048). These fields were chosen as representative of the crowding variations over the LMC fields. The stars were given fluxes according to randomly chosen microlensing events (one per artificial star). Reference xm images were created using these images and photometry performed in the same manner as for the normal (lm) images.

After photometry, the light curves of xm objects falling near artificial stars were studied to find values of the α_i . In practice, one median value of α was calculated for each lightcurve using points for which $(A - 1)_{\text{input}} > 0.5$, though no nonlinearity was observed that made this a crucial point. Of the 8000 artificial stars that were added to each of the four fields, most are not usable for various (understandable) reasons: star in a masked region of the CCD, event during a period with no observations, or the reconstructed magnitude not satisfying the Bright Sample cuts. For the field xm009, a total of 1123 lightcurves were usable for determining α . Of these lightcurves, 982 concerned objects for which the artificial star is the primary component, while in the remaining 141 objects the artificial star falls underneath a preexisting bright object on the original image. We use the first type of object to determine the distribution of α_1 , the value of α for the primary star associated with each object.

Figure 4 (top) shows the distribution of α_1 for the dense field lm009 and the sparse field lm048. The other two fields give similar distributions. The distributions of α_1 are characterized by

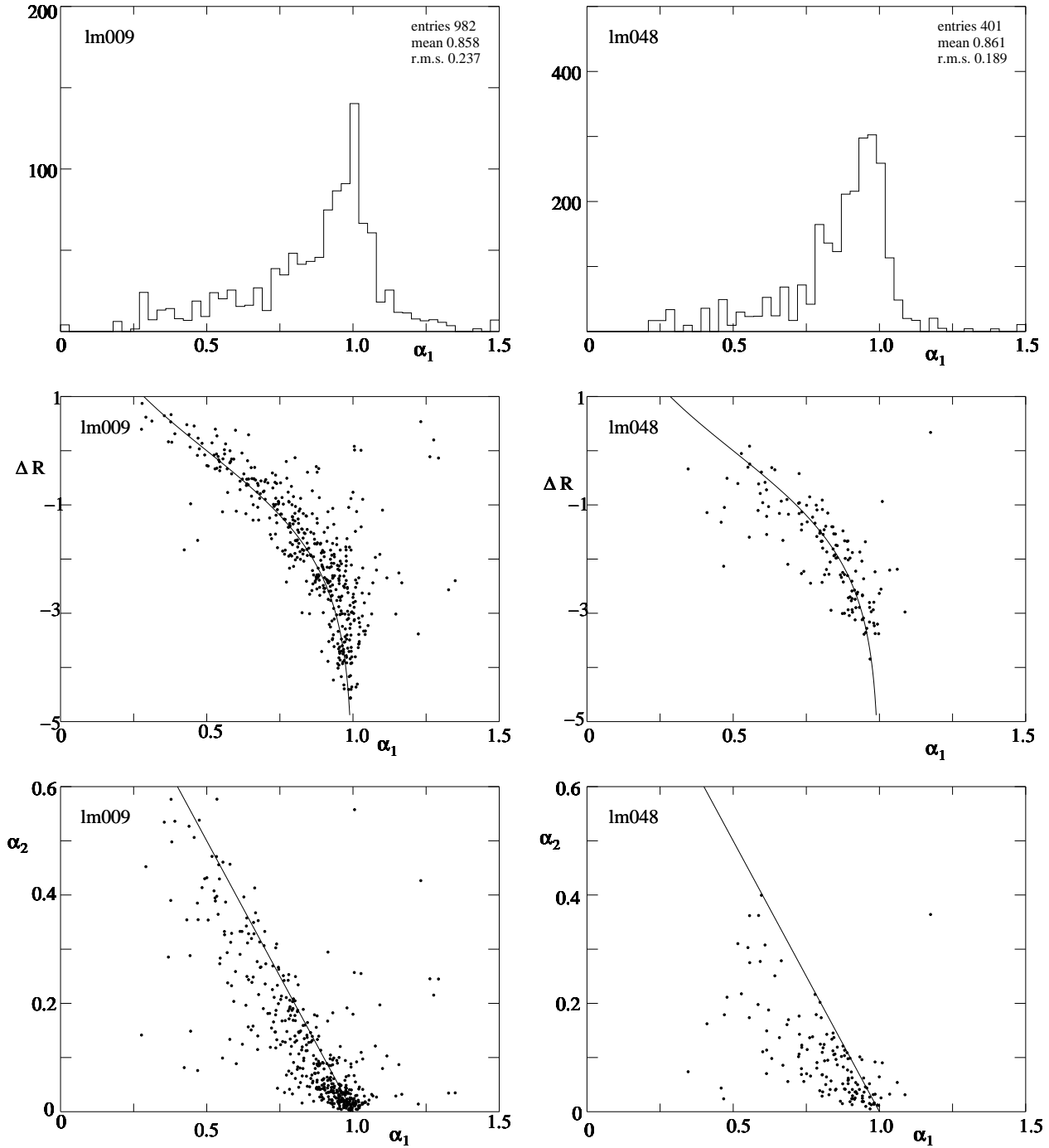


Fig. 4. The effects of blending on artificial stars added to the dense field Im009 (left) and the sparse field Im048 (right). The top two panels show the distribution of α_1 using artificial stars that do not fall under a brighter pre-existing object. Stars further than 2 arcsec from the nearest pre-existing object are concentrated in the peak at $\alpha_1 \sim 1$ while stars nearer to pre-existing objects form the tail at $\alpha_1 < 1$. The middle two panels show, for objects within 2 arcsec of pre-existing objects, the correlation between α_1 and the difference in magnitude between the artificial star and the pre-existing object. Artificial objects with α_1 significantly below unity are associated with pre-existing objects of similar magnitude. The line shows the expected relation for two superimposed objects: $\alpha_1 = 1 / (1 + 10^{0.4\Delta R})$. The bottom two panels show the distribution of (α_1, α_2) with α_2 calculated from (12) and the magnitude of the pre-existing object. The line shows the expected relation for two superimposed objects: $\alpha_1 + \alpha_2 = 1$.

peaks at $\alpha_1 \sim 1$ due to artificial stars falling more than ~ 2 arcsec from any pre-existing Im object. This happens for about half the artificial stars in the densest field (Im009) so blending has little effect on about half the bright stars in dense fields. Stars falling on pre-existing stars yield the tail at $\alpha_1 < 1$. This can be seen in the middle plots that show, for artificial stars within 2 arcsec of

pre-existing stars, the correlation between α_1 and the magnitude difference between artificial and pre-existing stars. The distribution follows closely the expected form $\alpha_1 = 1 / (1 + f_2 / f_1)$ where f_1 is the flux of the artificial star and f_2 is the flux of the preexisting star. For example, when $\alpha_1 \sim 0.5$ the cloud of points passes near $\Delta R \sim 0$.

The mean value of α_1 is ~ 0.86 equivalent to a mean value of u_1 of 0.92. This means that the (efficiency uncorrected) rate of events with amplifications of the primary component greater than 1.34 is reduced by a factor 0.92 from the rate calculated assuming no blending.

The loss of 8% of the events is compensated by extra events due to stars under the primary component. Since $\alpha_1 \sim 1/(1 + f_2/f_1)$, we can expect that $\alpha_2 \sim 1/(1 + f_1/f_2)$ for superimposed objects. However, the superposition is not perfect so α_2 must be a decreasing function of the separation between the object and star 2. The artificial events due to artificial stars falling under brighter pre-existing objects are well described by

$$\alpha_2(d) \sim \frac{f_2}{f_1 + f_2} \exp[-(d/d_0)^2] \quad d_0 = 1.9 \text{ arcsec} \quad (12)$$

where f_1 is the flux of the major component, f_2 is the flux of the minor (amplified) component and d is the separation between the xm object and the minor component. This formula can then be applied to the objects where the artificial star is the major component since the flux and position of the minor component (on the original image) is known. In the bottom panels of figure 4 we show α_1 vs. α_2 for the fields lm009 and lm048. The anticorrelation between α_1 and α_2 means that the loss of events due to $\alpha_1 < 1$ is partially compensated by events from the second star on an object by object basis.

The compensation is seen in figure 5 histogramming u_1 and $u_1 + u_2$. The sum $u_1 + u_2$ gives the rate for event with amplifications > 1.34 compared to that calculated assuming $\alpha = 1$. In lm048, events due to the second star compensate for the loss of events on the first star while in the dense field lm009 there is a 10% overcompensation. As we will see in Section 7, the efficiency to observe the blended events is degraded compared to unblended events, so the overall number of expected events is about 10% less than what one would calculate ignoring blending.

We have checked our calculations by studying public HST images of a small part of the densest EROS region, that of lm009 ccd 3. A catalog of stars for this region was produced and images with EROS seeing were fabricated. As in the previous analysis, images with some amplifications were compared with reference images. Figure 5 shows the distribution of u_1 for bright objects on the convoluted images. Because of the very high density of stars, u_1 is somewhat smaller than that calculated with the artificial images: $\langle u_1 \rangle = 0.85$ as opposed to $\langle u_1 \rangle = 0.92$. This lower value of u_1 is, as expected, compensated by higher values of u_2 . Figure 5 shows the histogram of $u_1 + u_2$ indicating that the event rate is raised by 15% over the unblended rate. Including the loss of efficiency modifies this so that the event rate is only 5% higher than the unblended rate.

4. Candidate selection from the Bright-Star Sample

The present analysis aims at detecting luminosity excursions, due to microlensing, on otherwise constant light curves. The smallest reachable microlensing timescale, t_E , is determined by the sampling of the fields; in practice, except for a few fields, the detection efficiency is very low below 2-3 days. The largest detectable timescale, about 800 days, is determined by the reduction in the detection efficiency when the timescale becomes so large that the baseline flux is not seen during the observing period.

The analysis is guided using the simulation of microlensing described in Section 7, which also serves to determine the efficiency of the selection procedure.

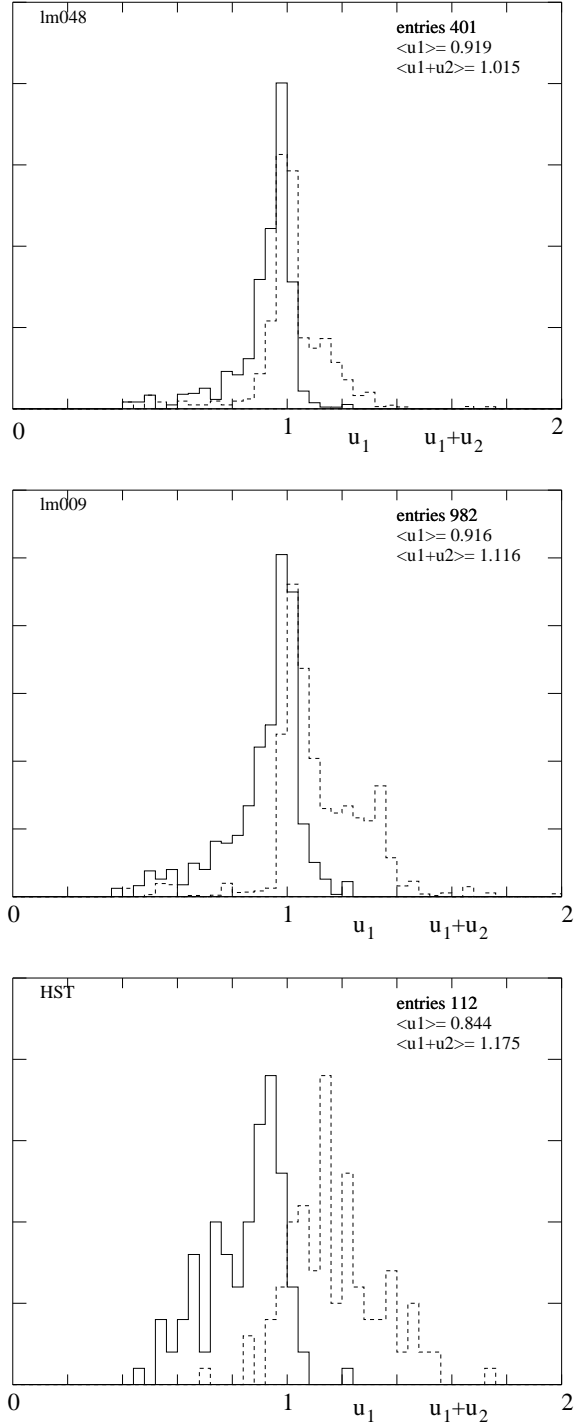


Fig. 5. The distribution of u_1 (solid line) and $(u_1 + u_2)$ dashed line for the sparse EROS field lm048 (top panel) the dense EROS field lm009 (middle panel) and the very dense HST field in lm009, ccd3 (bottom panel) as described in the text. The distributions of u_1 are all characterized by a peak near $u_1 \sim 1$ and a tail at $u_1 < 1$. With increasing star density, the mean of $u_1 + u_2$ increases because of the increasing importance of secondary stars.

In the present analysis, luminosity excursions are defined with respect to the baseline stellar flux; the first task is thus to determine this baseline. To that end, we order the N measured fluxes Φ_i of the light curve by increasing values of Φ . For each of the $N - 1$ middle values of the flux intervals $\Phi_{i,mid} = 0.5(\Phi_i + \Phi_{i+1})$, we count the number $N_{run,i}$ of runs, i.e. groups of

cut	LMC	SMC
Bright-Star Sample	6052102	900809
Filter (C1, C2, C3)	33876	5787
$LP_{N,pos,1}/LP_{N,pos,2} > 10$ (C4)	6778	847
good χ^2_{base} (C5)	2636	266
t_0 (C6)	2065	195
$N_{peak} > 4$ (C7)	1624	149
significant $\Delta\chi^2$ (C8)	350	32
good χ^2_{peak} (C9)	152	17
BlueBumper (C10)	10	4
SN ($S < 0.3$) (C11)	7	4
$u_0 < 1$ (C12)	1(SN)	1

Table 1. The number of light curves surviving the cuts C1 to C12 as described in the text.

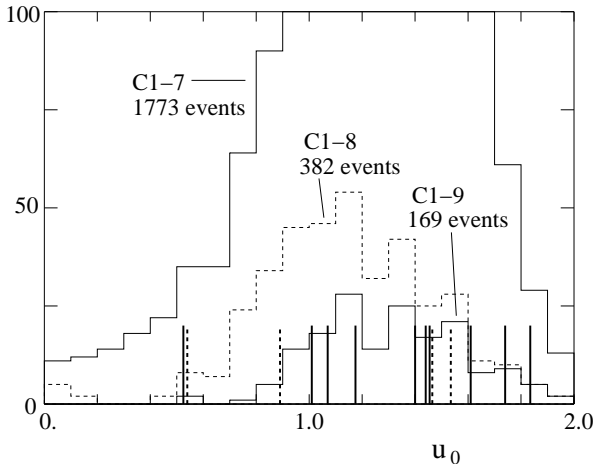


Fig. 6. The u_0 (mean of those for R_{eros} and B_{eros}) distribution for LMC and SMC light curves surviving cuts C1-C7, C1-C8, and C1-C9. The positions of the 14 light curves surviving cuts C1-C10 are shown with the 4 supernovae as dashed lines.

consecutive points on the light curve that are on the same side of $\Phi_{i,mid}$.⁸ The baseline flux is defined as that value of $\Phi_{i,mid}$ which maximizes $N_{run,i}$. This way of defining the baseline has a precision similar to that of a simple average of the fluxes, but it proves much more robust to aberrant measurements, and less biased for most variable stars. We have checked on the simulated microlensing light curves that there is no visible bias for timescales t_E shorter than ~ 200 d. The bias is non-negligible above 600 d, but this is taken into account in the efficiency calculation.

Next, we determine the point-to-point dispersion in the light curve σ_{ptp} , from the comparison of each measured flux with the linear interpolation of its two neighboring (in time) fluxes. This is done separately for the 7 seasons of data taking, as we have observed a progressive degradation of the photometric scatter in the last 3 seasons.

Using the baseline flux and the photometric scatter, we then search for luminosity excursions defined as a group of consecutive points with fluxes sufficiently far from the baseline flux. These should have at least 5 consecutive measurements more than $1.5\sigma_{ptp}$ from the baseline. In practice, to increase the de-

⁸ Or, equivalently, $N_{run,i}$ is the number of times the time-ordered light curve crosses the constant flux line at $\Phi_{i,mid}$, plus one.

tection efficiency for short duration phenomena, we allow small “holes” within the excursion (series of points less than $1.5\sigma_{ptp}$ from the baseline) provided that each hole contains exactly one measurement. We call positive (negative) excursions those comprised of fluxes higher (lower) than the baseline.

The relative significance of each excursion is then estimated using the probability that it corresponds to a statistical fluctuation of a normal law. We use the variable LP_N , the co-logarithm of this probability

$$LP_N = - \sum_{i=1}^{i=N} \log \left(\frac{1}{2} \operatorname{Erfc} \left(\frac{x_i}{\sqrt{2}} \right) \right),$$

where x_i is the deviation from the baseline of the point taken at time t_i , in units of its error σ_i , and N is the number of points within the excursion. The excursions are ranked by decreasing values of LP_N (decreasing significance).

We now describe the 12 selection criteria, C1-C12, used to select microlensing candidates. C1 requires at least one significant positive excursion:

$$C1 : LP_{N,pos,1} > 20 .$$

The largest negative excursion should be much smaller than the largest positive one:

$$C2 : LP_{N,pos,1}/LP_{N,neg,1} > 10 .$$

There should be less than 10 excursions in total:

$$C3 : N_{excursions} < 10 .$$

Cuts C1, C2 and C3 are applied independently in the two passbands and a star is retained for further analysis only if it passes the three cuts in both bands. There are 33876 LMC light curves and 5787 SMC light curves that survive. The progression of the number of surviving light curves with the subsequent cuts is shown in Table 1.

All light curves passing C1 – 3 are fitted with a simple microlensing curve (10), independently in the two passbands. The results of the fits, i.e. the fitted parameters t_0 , u_0 and t_E and the values of χ^2 , are used in cuts C5-C10.

Cuts C4 and C5 eliminate light curves with significant variability outside the main positive excursion. We first require that the second positive excursion be much less significant than the first one:

$$C4 : LP_{N,pos,1}/LP_{N,pos,2} > 10 .$$

To discriminate against low amplitude variations (either real or due to photometric problems) we require that the normalized χ^2_{base} for a time independent light curve outside the main excursion (points with $u > 2$) be sufficiently good:

$$C5 : \frac{\chi^2_{base} - N_{dof,base}}{\sqrt{2N_{dof,base}}} < 20 .$$

This cut may seem loose as it would correspond to cuts at 20 standard deviations, for a normal law. However, the errors we use to compute χ^2_{norm} are only estimates of the actual errors. For isolated stars, the errors are overestimated. The values of the cuts have thus been tuned using the simulated light curves, that have the same uncertainties as the original data; the two cuts reject about 10% of the simulated microlensing light curves.

Cuts C6 and C7 require that the main fluctuation occur at a time when the light curve is sufficiently well sampled. In order

to discriminate against stellar variations with very asymmetric peaks we thus require that the time t_0 be within the observing interval:

$$C6: \quad T_{beg} + t_E < t_0 < T_{end} - t_E,$$

where T_{beg} and T_{end} are the first and last date of EROS-2 observations. We also require that there be more than 4 flux measurements within the main fluctuation ($u < 2$)

$$C7: \quad N_{peak} > 4.$$

There are 1624 LMC light curves and 149 SMC light curves that survive cuts C1-C7. Their distribution of u_0 and those of light curves satisfying subsequent cuts are shown in Figure 6. It is seen that most light curves show only low amplitude variations with $u_0 > 0.6$.

We next require that the microlensing fit to the light curves in both passbands be significantly better than the fit of a constant flux:

$$C8: \quad \frac{\chi_{ct}^2 - \chi_{ml}^2}{\chi_{ml}^2 / N_{dof}} \frac{1}{\sqrt{2N_{dof,peak}}} > 40,$$

where χ_{ct}^2 and χ_{ml}^2 are the chi-squared values for the constant fit and the simple microlensing fits, and N_{dof} and $N_{dof,peak}$ are the number of measured points in the full light curve and in the peak. The event is required to pass this cut in both passbands. This cut eliminates light curves that have low amplifications, poor sampling, and/or poor photometric errors.

We then require a reasonably good fit to the microlensing curve within the peak:

$$C9: \quad \frac{\chi_{peak}^2 - N_{dof,peak}}{\sqrt{2N_{dof,peak}}} < 10.$$

There are 152 LMC and 17 SMC light curves that pass cuts C1-C9. As can be seen in Figure 6, almost all of these light curves have $u_0 > 0.8$. They are mostly bright main-sequence stars that display low-amplitude variations that are difficult to distinguish from microlensing, though they often show $\sim 20\%$ more variation in the red than in the blue. They were first mentioned in Alcock et al. (1997a) and are commonly called ‘‘blue bumpers’’.

We identify blue bumpers first from their position in the color-magnitude diagram and their low, chromatic amplification. For stars with $(B - R)_{eros} < 0.2$ and $R_{eros} < 18.6$ (LMC) or $R_{eros} < 18.9$ (SMC), we require

$$C10: \quad \min(A_R, A_B) > 1.6 \quad \text{and} \quad \frac{A_R - 1}{A_B - 1} < 1.2,$$

where A_R and A_B are the maximum amplifications observed in the two bands. These two amplifications are taken to be the fitted amplifications at the time of the maximum *observed* amplification. This value is used since the fitted amplification at $t = t_0$ may significantly overestimate a blue bumper amplitude if the peak region is not well sampled.

There are 10 LMC light curves and 4 SMC light curves that pass cuts C1-C10. Four of these light curves are most likely supernovae (SN) exploding in galaxies far behind the Magellanic Clouds. In the analysis of the Full Sample of EROS-2 Magellanic light curves (Tisserand 2004), 31 such supernovae were found. All SN in our sample have fitted timescales in the range 25-50 days, asymmetric light curves with a faster rise time, and larger variations in the bluer passband. For a fraction of

them, about 20%, the host galaxy is visible, which makes them indisputable SN. In order to identify the remaining SN, we have devised a fitting function with a time asymmetry parameter S ; the function reduces to simple microlensing for $S = 0$. The fitting function is obtained from simple microlensing (10) by replacing the Einstein timescale t_E by the ‘‘supernova’’ varying timescale

$$t_S = t_E \left[1 + S \arctan\left(\frac{t - t_0}{t_E}\right) \right]. \quad (13)$$

For positive (negative) values of S , the rise time is faster (slower) than the decrease time. When fitting this function to the remaining light curves, we expect to find $S > 0$ for the SN. Based on the study of the supernovae found in the Full Sample analysis and on simulated microlensing events, we choose to eliminate light curves with blue-band asymmetries by requiring

$$C11: \quad S_b < 0.30.$$

This cut eliminates 3 light curves from the Bright-Star Sample, leaving 11 light curves, mostly with very small amplitudes, $u_0 > 1$. Since the u_0 distribution for microlensing events is flat, the events with $u_0 > 1$ in Figure 6 must be mostly background. We therefore require

$$C12: \quad u_0 < 1.0.$$

This leaves two light curves. One of them is superimposed on a clear background galaxy. It is therefore most likely a supernova and we eliminate this event leaving one event to be discussed in the next section.

5. Candidate sample and verifications

After the cuts described in the previous two sections have been applied, only one candidate microlensing event remains in the Bright-Star Sample, EROS2-SMC-1. Its light curve is shown in fig. 7 and its characteristics are given on the first entry in Table 2. It has been known since 1997 (Alcock et al. 1997b; Palanque-Delabrouille et al. 1998) and is identical to candidate MACHO-97-SMC-1. It has one of the two longest timescales (103 d) and the highest luminosity of all published microlensing candidates reported toward the Magellanic Clouds. The star is separated by 1.6 arcsec from another star that is 1.2 mag fainter (Udalski et al, 1997) causing $\sim 30\%$ blending in EROS-2 images. Including the blend in the light curve fit increases t_E to 125 d.⁹ The star displays a 4-5% variability with a period $P = 5.12$ d (Palanque-Delabrouille et al. 1998). For further details on this event, see Palanque-Delabrouille et al. (1998), Afonso et al. (1999, 2003a) and Assef et al. (2006).

As a check on the cuts C1 – 12 leading to EROS2-SMC-1 and to search for nonstandard microlensing events (e.g. those due to binary lenses), a large number of light curves were visually scanned. Among them were all events satisfying C1-C8 and $u_0 < 1$, all events satisfying C1-C7 and $u_0 < 0.5$, all events satisfying C1-C10, and all events satisfying C1-C12 but with R_{max} increased by 0.2 mag. Only one interesting event was found, EROS2-LMC-15 shown in Figure 8. The beginning of the event is very similar to a standard microlensing event but subsequent points are too high.¹⁰ It was rejected by the χ_{peak}^2 cut (C9) but it

⁹ When blending is taken into account, this event has the longest t_E of any published Magellanic event.

¹⁰ OGLE-3 data confirm the high flux of the post-peak points (A. Udalski, private communication).

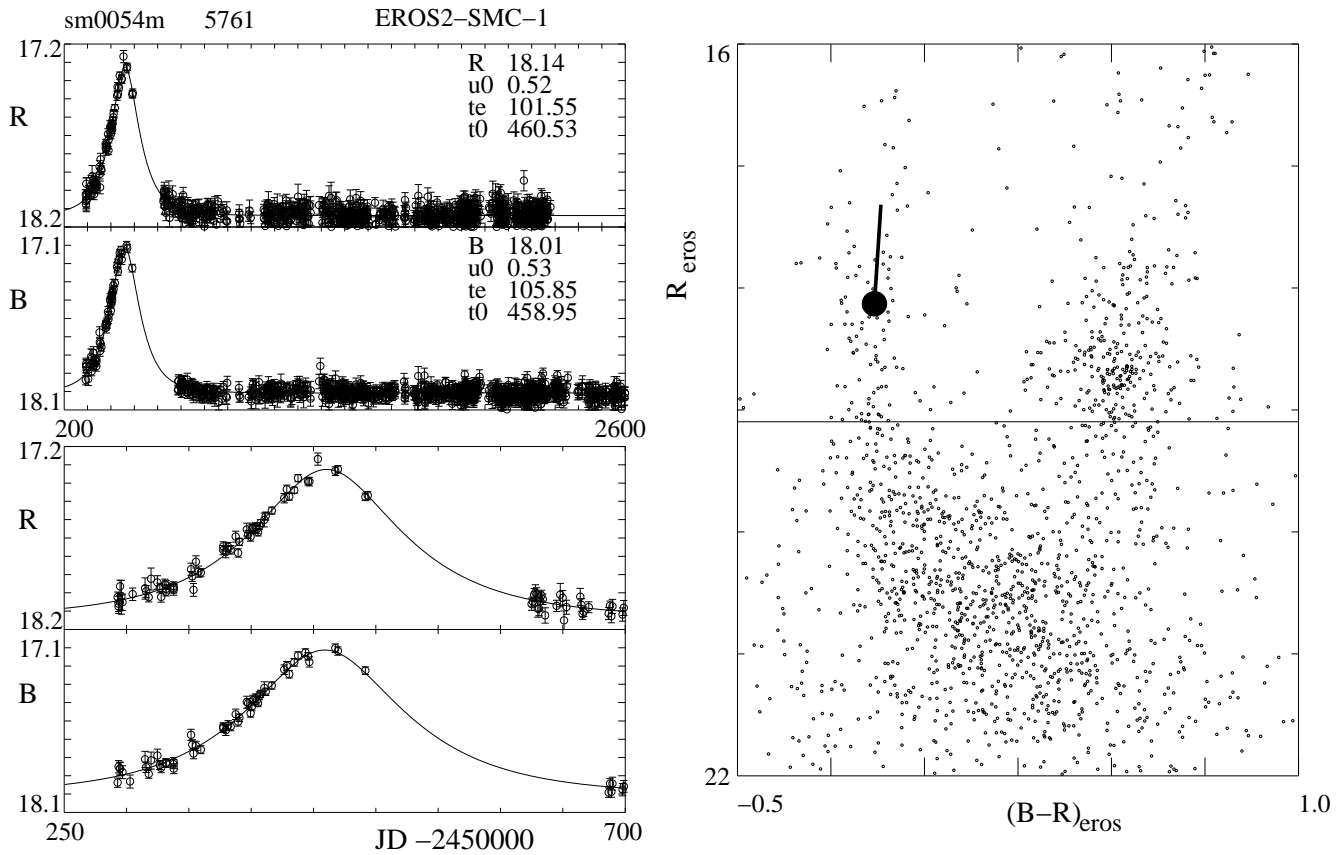


Fig. 7. The light curves of EROS-2 microlensing candidate EROS2-SMC-1 (star sm005-4m-5761). Also shown is the color-magnitude diagram of the star's CCD-quadrant and the excursion of the event.

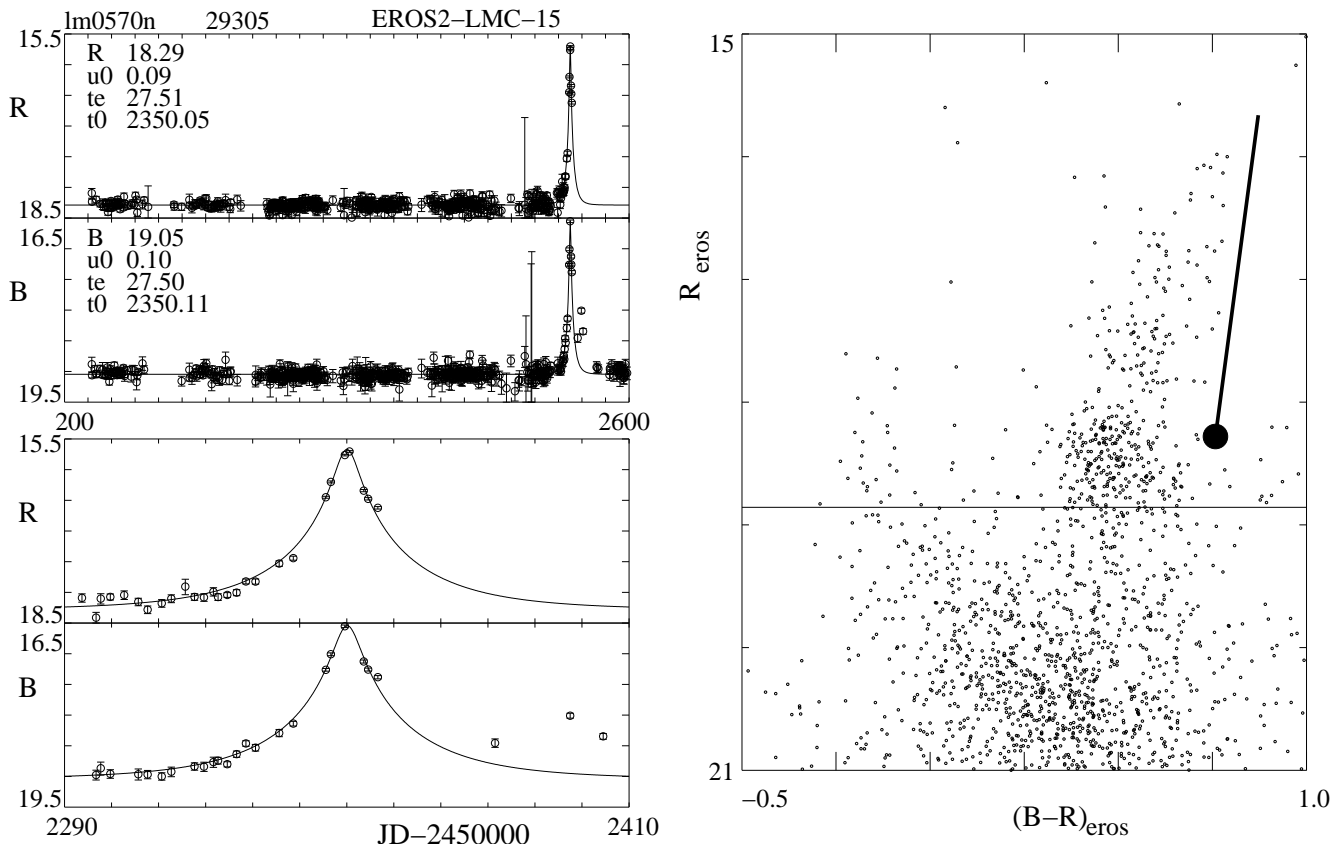


Fig. 8. The light curves of EROS-2 star lm057-0n-29305 (r.a.= 79.9488 deg, dec.= -70.7741 deg). Also shown is the color-magnitude diagram of the star's CCD-quadrant and the excursion of the event.

candidate	EROS-2 star	r.a. (deg)	dec. (deg)	R_{eros}	$(B - R)_{\text{eros}}$	t_0	t_E	u_0	χ^2/dof
EROS2-SMC-1	sm005-4m-5761	15.0233	-72.2507	18.14	-0.13	459.0	105.8	0.53	972.4/873
						460.5	101.6	0.52	862.4/748
EROS2-SMC-5	sm006-6k-19475	12.6625	-72.6983	17.83	0.34	1414.8	29.5	0.90	485.1/875
						1432.0	15.1	1.12	560.0/573
EROS2-LMC-8	lm055-7m-23303	76.6396	-71.6624	20.34	1.16	1594.1	15.3	0.01	344.0/572
						1594.1	8.0	0.03	540.9/510
EROS2-LMC-9	lm042-11-2622	75.3717	-65.0486	20.93	0.23	2204.1	57.8	0.36	640.8/369
						2215.3	52.7	0.30	292.1/228
EROS2-LMC-10	lm045-5n-26323	80.9925	-65.8733	20.55	0.81	1600.3	37.1	0.33	580.0/505
						1602.2	35.9	0.51	649.1/447
EROS2-LMC-11	lm061-4m-15782	88.4392	-71.2536	20.55	0.55	451.9	51.3	0.36	456.5/444
						446.6	46.1	0.37	458.7/394
EROS2-LMC-12	lm085-6l-14234	89.8750	-74.5676	20.19	0.34	2664.0	49.6	0.27	580.4/391

Table 2. Events found in the analysis of the full sample of EROS-2 stars (Tisserand 2004). Only event EROS2-SMC-1 is in the Bright-Star Sample and passes the cuts C1-C12 and therefore is used for limits on the optical depth. All fits assume zero blending and no intrinsic variability. The two values of the fitted parameters t_0 , t_E and u_0 are for B_{eros} (first line) and R_{eros} (second line). (There are no R_{eros} points during the event for EROS2-LMC-12.) The time of maximum, t_0 is given as JD-2450000.

may, in fact, be a lensing event due to a binary lens. Note that its position in the color-magnitude diagram suggests that the star is either not in the LMC or behind a foreground Milky Way star.

An important verification of the analysis of the Bright-Star Sample presented here comes from an analysis of the Full Sample of Magellanic light curves described in Tisserand (2004). Because faint stars were analyzed, the cuts, given in Appendix A, were generally slightly stricter than those described in Section 4. However, the analysis did not require observation of the event in both colors. It therefore provides an important check on our analysis. The candidates found in this analysis are listed in Table 2 and their light curves shown in Appendix A. Two candidates EROS2-SMC-1 and 5 are in the Bright-Star Sample. Candidate 5 does not pass the cuts presented here because it fails C12. We also note that it shows non-microlensing-like variations in the light curve of the MACHO collaboration¹¹.

Two other independent analyses were performed on the SMC data, restricted to the first five years of data. In both cases, the only event found in the Bright-Star Sample was EROS2-SMC-1. The first analysis, reported in Afonso et al. (2003a), was based on a larger set of stars (5.2 million); the number of analysis cuts common to it and the present analysis is small; the computer programs were written independently. The second analysis followed a complete reprocessing using a new implementation of differential photometry developed by Le Guillou (2003). The technique would allow us to find events not on cataloged stars.

We attempted to check our efficiency for finding microlensing events by considering the events published by the MACHO collaboration. The 13-17 events (Alcock et al. 2000b) used by them to measure the optical depth toward the LMC are listed in Table 3. Only 2 of the 17 stars (MACHO-LMC-18 and 25) are bright enough to be in our Bright-Star Sample. Three of the 17 events occurred after the beginning of EROS-2 operations but none of these three events occurred on stars in our Bright-Star Sample. One of the three (MACHO-LMC-15) was on a star too dim to be seen by EROS-2.¹² The two other events

¹¹ <http://www.macho.mcmaster.ca/Data/MachoData.html>. There is no information at this site on the EROS-2 LMC candidates of Table 2 since none are in MACHO fields.

¹² The 1.27 m telescope of the MACHO collaboration allowed them to use fainter stars than EROS-2 with its 1 m telescope.

(MACHO-LMC-14 and 20) are seen in the EROS-2 images and give microlensing parameters compatible with those measured by MACHO (see Table 3).

MACHO-LMC-14 was selected in the MACHO A analysis. In EROS-2, it was located in a defective zone of 200 x 2000 pixels on CCD 7 of our blue camera, near the edge of the mosaic. The corresponding star was not cataloged in this band, and the star failed the requirement to be observed in both passbands. Consequently, it does not appear in Table 2.

MACHO-LMC-20 was selected in the MACHO B analysis. In EROS-2, it is located 35 arcsec from a very bright Galactic star (about $V = 10$ vs. 21 for the candidate). In this analysis, stars too near bright stars were eliminated so this candidate does not appear in Table 2.

6. The status of published Magellanic microlensing candidates

In this section, we review and update the status of the published Magellanic microlensing candidates of the EROS and MACHO collaborations.

EROS has, in the past, used 11 candidates to place upper limits on the optical depth toward the LMC and to measure the depth toward the SMC. Six of the candidates are in the Bright-Star Sample considered here. The candidates and their present status are given in Table 4.

Of the candidates in Table 4 only EROS2-SMC-1 remains as a candidate microlensing event. The others have been eliminated either because continued observations of the same stars show further variability on the light curves, or because improved photometry, in some cases complemented by spectroscopy, lead to re-interpreting the candidates as variable stars. Before the analysis presented here, the following EROS candidates were eliminated: EROS1-LMC-2, presented in Aubourg et al. (1993) and which displayed a new variation 8 years later (Lasserre et al. 2000); and candidate EROS2-LMC-4, presented in Lasserre et al. (2000) and eliminated in Milsztajn et al. (2001).

Before this analysis started, there were 5 surviving LMC microlensing candidates from EROS, one from EROS-1 (num-

MACHO candidate	EROS-2 star	R_{eros}	$(B - R)_{\text{eros}}$	t_0	t_E	A_{max}	comments
MACHO-LMC-1	lm019-6k-14879	18.97	0.61	-942.9	17.20	7.15	
MACHO-LMC-4	lm057-0l-27696	19.85	0.24	-353.1	22.70	2.92	
MACHO-LMC-5	lm057-0k-27469	19.97	1.52	-976.1	37.80	47.28	
MACHO-LMC-6	too faint			-802.9	45.80	2.43	
MACHO-LMC-7	lm010-2k-21383	20.47	0.52	-536.5	51.45	5.91	
MACHO-LMC-8	too faint			-612.2	33.20	2.19	
MACHO-LMC-9 B-binary	lm001-0l-6864	20.92	0.83	-400.1	89.60	1.95	
MACHO-LMC-13	lm020-6m-19733	21.03	-0.07	134.0	50.05	2.36	
MACHO-LMC-14	lm002-7n-24616	18.84		391.3	50.05 (38.2)	3.37 (2.77)	
MACHO-LMC-15	too faint			472.4	18.40	2.83	
MACHO-LMC-18	lm060-2n-16057	18.35	0.47	-217.2	37.10	1.54	Bright Sample
MACHO-LMC-20 B	lm012-5n-23157	20.09	1.03	774.7	36.35 (23.2)	2.95 (3.1)	
MACHO-LMC-21	dead zone			-786.8	46.60	5.64	
MACHO-LMC-22 B	dead zone			-43.3	114.65	2.70	
MACHO-LMC-23	lm055-3n-4994	19.82	0.37	-237.7	42.60	2.41	variable (Fig. 10)
MACHO-LMC-25	lm017-2m-2056	17.95		-265.7	42.60	1.50	Bright Sample
MACHO-LMC-27 B	lm010-0n-23830	19.00	0.14	-485.9	25.25	1.45	

Table 3. The 17 microlensing candidates of the MACHO collaboration (Alcock et al. 2000b). Candidates 20, 22 and 27 (marked B) are low signal-to-noise candidates not satisfying the MACHO “A” requirements. Candidate 9 is due to a binary lens and does not satisfy their A requirements. The values of t_E and maximum amplification A_{max} are from the MACHO fit assuming no blending, and t_0 is given as JD-2450000. Candidates 18 and 25 are each within 1 arcsec of an object of similar magnitude that is resolved by the MACHO analysis but blended in the EROS analysis. Candidates 14 and 20 occurred during EROS-2 observations, and the EROS-2 values of t_E and A_{max} are shown in parentheses (averages of R_{eros} and B_{eros} measurements).

Candidate	EROS-2 star	R_{eros}	$(B - R)_{\text{eros}}$	original ref.	status
EROS1-LMC-1	lm058-2k-21915	18.75	0.34	Aubourg et al. (1993)	2 nd variation (Tisserand 2004) (Figure 9)
EROS1-LMC-2	lm043-6m- 9377 B-S	19.32	-0.04	Aubourg et al. (1993)	2 nd variation (Lasserre et al. 2000)
EROS2-LMC-3	lm034-6l-20493	20.90	0.61	Lasserre et al. (2000)	2 nd variation (Tisserand 2004)
EROS2-LMC-4	lm018-6n-23236	19.10	1.87	Lasserre et al. (2000)	2 nd variation (Milsztajn et al. 2001)
EROS2-LMC-5	lm015-3n-22431 B-S	19.17	0.14	Milsztajn et al. (2001)	Supernova (Tisserand 2004)
EROS2-LMC-6	lm067-5m-14700	21.01	0.63	Milsztajn et al. (2001)	Supernova (Tisserand 2004)
EROS2-LMC-7	lm070-3n-23389	21.00	0.76	Milsztajn et al. (2001)	Supernova (Tisserand 2004)
EROS2-SMC-1	sm005-4m-5761 B-S	18.13	-0.13	Palanque-D. et al.(1998)	Fig. 7
EROS2-SMC-2	sm001-6l-13221 B-S	19.56	0.44	Afonso et al. (2003a)	long period variable (Tisserand 2004)
EROS2-SMC-3	sm001-6n-16904 B-S	19.31	0.59	Afonso et al. (2003a)	long period variable (Tisserand 2004)
EROS2-SMC-4	sm002-7m-21331 B-S	19.48	0.32	Afonso et al. (2003a)	long period variable (Tisserand 2004)

Table 4. The 11 events of the EROS collaboration used in the past to set upper limits on the microlensing optical depth toward the LMC and to measure the depth toward the SMC. Candidates marked “B-S” in column 2 occur on stars in the EROS-2 Bright-Star Sample. All candidates except EROS2-SMC-1 have been eliminated as variable stars or as supernovae.

ber EROS1-LMC-1) and four from EROS-2 (numbered EROS2-LMC-3, 5, 6 and 7).

The EROS-1 candidate EROS1-LMC-1 displayed a new variation in the EROS-2 data (Figure 9) in 1998, 6.3 years after the first one, of similar amplitude (a factor two) and timescale (27 days). This second variation is well fitted by a microlensing light curve. Because they are separated in time by more than 80 Einstein timescales, the probability that these two bumps correspond to the microlensing of a double source star is lower than half a percent, even in the favorable case of the two stars being of equal luminosity. This candidate was thus rejected. Let us recall that it was already known to be a Be star (Beaulieu et al. 1995) and was thus already suspected of being variable (Paczynski 1996). Candidate EROS2-LMC-3 also displayed new variations

between 1999 and 2002, of a more irregular nature, and was thus rejected.

The light curves of candidates EROS2-LMC-5, 6 and 7 have been improved, due to the better template images in the present analysis. The reduced photometric scatter, compared to Milsztajn et al. (2001), made apparent an asymmetry in rise and fall times; the asymmetry test (C11) allowed us to identify and reject them as supernovae. EROS2-LMC-5 is identical to MACHO-LMC-26, which had been rejected by Alcock et al. (2000b) for the same reason.

The conclusion is that *none* of the former EROS LMC microlensing candidates are still considered valid. Four displayed further variability, and three were identified as SN thanks to improved photometry.

There have been four EROS-2 SMC candidates, EROS2-SMC-1 discussed in Section 5, and EROS2-SMC-2, 3 and 4 presented in Afonso et al. (2003a). Candidates 2, 3 and 4 were described as doubtful candidates, as all three display very long timescale variations, and look more like irregular variable stars. Another analysis of the same SMC data using differential photometry (Le Guillou 2003) allowed us to reduce the photometric errors and substantiate this interpretation. The additional two years of data since Afonso et al. (2003a) have confirmed this, as further irregular variations have been observed. They are not selected in the present analysis, and are now considered as definitively rejected.

We have also searched for further variations in the 17 stars used by the MACHO collaboration to measure the optical depth toward the LMC (Table 3). One of the candidates, MACHO-LMC-23, showed a further variation in the EROS-2 data (Tisserand 2004), 6.8 years after its first variation in the MACHO data. Its EROS-2 lightcurve is shown in Figure 10. As such, we can eliminate it as a microlensing candidate. In spite of this, both the variation shown in Figure 10 and the original variation in the MACHO data are quite achromatic, indicating that achromaticity is not a fool-proof criterion for selecting microlensing events. We note however that Bennett et al. (2005) argued that, even without considering its further variation seen in the EROS-2 data, the form of its light curve made MACHO-LMC-23 a weak microlensing candidate.

The MACHO collaboration has also reported candidate events found by their alert system. The most notable is MACHO99-LMC-2 that was studied by Bond et al. (2002). This impressive microlensing candidate was on a star too faint to be in the EROS Full Sample.

Besides the 17 LMC events of the MACHO collaboration, they have reported two candidates in the SMC, though they have reported no systematic search for SMC events. The first MACHO SMC candidate (Alcock et al. 1997b) is identical to EROS2-SMC-1 (Section 5). The second candidate, MACHO-98-SMC-1, concerned a star too faint to be included in our Full Sample of SMC stars. The event was detected by the alert system of the MACHO group in May 1998 and a probable caustic crossing due to a double lens was announced soon after. The source star was monitored by most microlensing groups, including EROS-2. The second caustic crossing was fully measured, which allowed the determination of the relative proper motion between the lens and source, allowing one to conclude that the event was due to a lens in the SMC (Afonso et al. 1998, 2000).

13

7. The detection efficiency

To measure the optical depth from the detected events, or limits on this quantity, we first need to evaluate the detection efficiency as a function of the time scale t_E . This was determined by using Monte Carlo simulated light curves : we superimpose artificial microlensing events on a representative sample of light curves, corresponding to 2% of the Bright-Star Sample from each of the 98 monitored fields. The light curve for a simple microlensing event (i.e. point-source point-lens zero-blending) is

¹³ Note that there exists a third, unpublished, microlensing candidate toward the SMC, OGLE-2005-SMC-001 (<http://bulge.astro.princeton.edu/~ogle/>). Its long timescale (> 150 d), large amplification (> 12) and bright source ($I = 18.2$) offer the prospect of completely resolving the microlensing parameters degeneracy through measurements of lightcurve deformations, e.g. of that due to parallax.

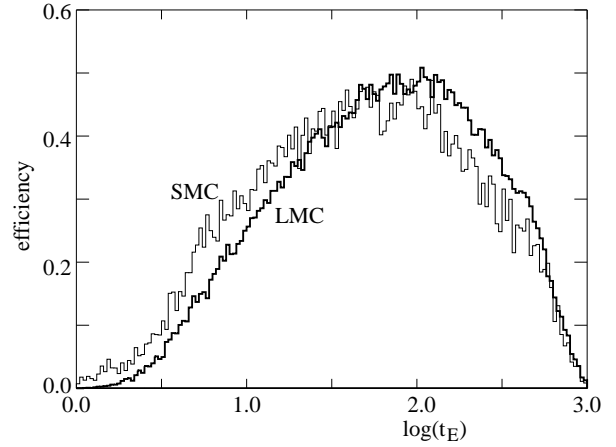


Fig. 11. The detection efficiency for unblended ($\alpha = 1$) microlensing light curves (10) as a function of t_E for LMC (bold line) and SMC (light line) fields. The efficiency applies to a 2500 d total observing period. The efficiency used for calculation of the optical depth is the efficiency shown here, multiplied by 0.9 to take into account lensing by binary lenses.

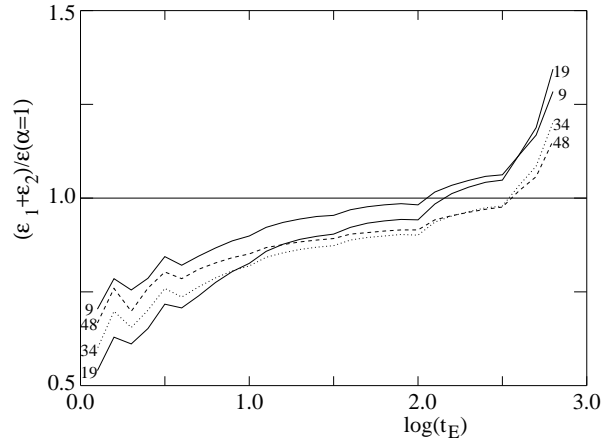


Fig. 12. The ratio between the summed efficiency, $\epsilon_1(\alpha_1) + \epsilon_2(\alpha_2)$ and the unblended efficiency $\epsilon(\alpha = 1)$ for pairs (α_1, α_2) taken from the artificial star analysis of Section 3. The ratio is a function of t_E . The four curves correspond to the four studied fields, lm009, 019, 034 and 048.

described by three parameters of (10): date of maximum amplification t_0 , impact parameter u_0 and time scale t_E . Blended events have the additional parameter α in (11). The microlensing parameters are chosen at random: t_0 follows a flat distribution over our 2500 days observing period, JD 2,450,242 till 2,452,742; u_0 is picked randomly between 0 and 1.2; and t_E is chosen at random from a distribution flat in $\ln(t_E)$, between 1 and 1000 days. Each star in the 2% sample is actually used thrice in the simulation, once per decade in t_E . The simulation takes into account the relative variation of photometric errors.

Simulated light curves were then fed into the analysis chain to find the fraction that are recovered by our detection algorithm. The detection efficiency in a given t_E bin, $\epsilon(t_E)$, is then given by the ratio between the number of events passing all selection criteria in this bin and the number of microlensing events generated in the same bin with $u_0 < 1$.

Figure 11 shows the LMC and SMC efficiencies for unblended events ($\alpha = 1$) as a function of t_E . For the range of

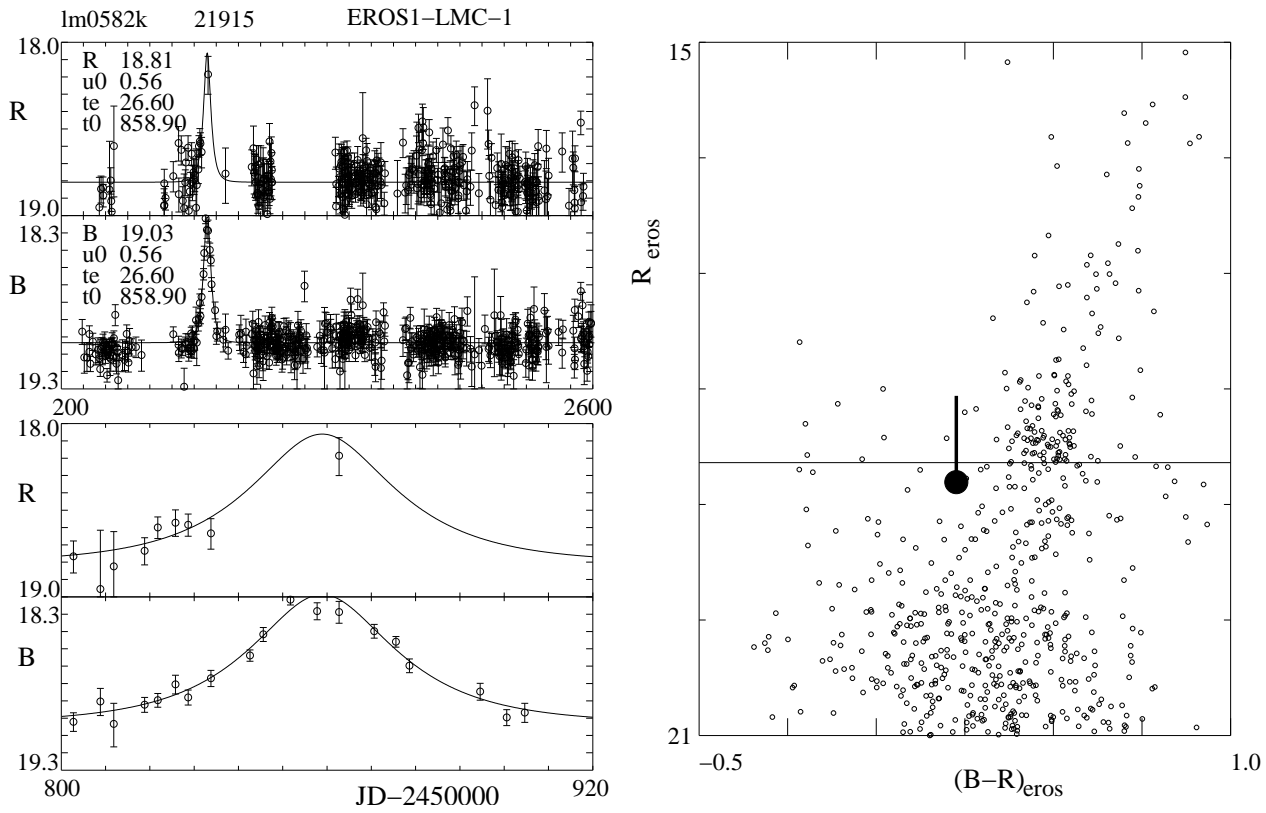


Fig. 9. The EROS-2 light curve of EROS-1 microlensing candidate EROS1-LMC-1. The curve shows a second variation, 6.3 years after the variation observed in EROS-1. Also shown is the color-magnitude diagram of the star’s CCD-quadrant and the excursion of the event.

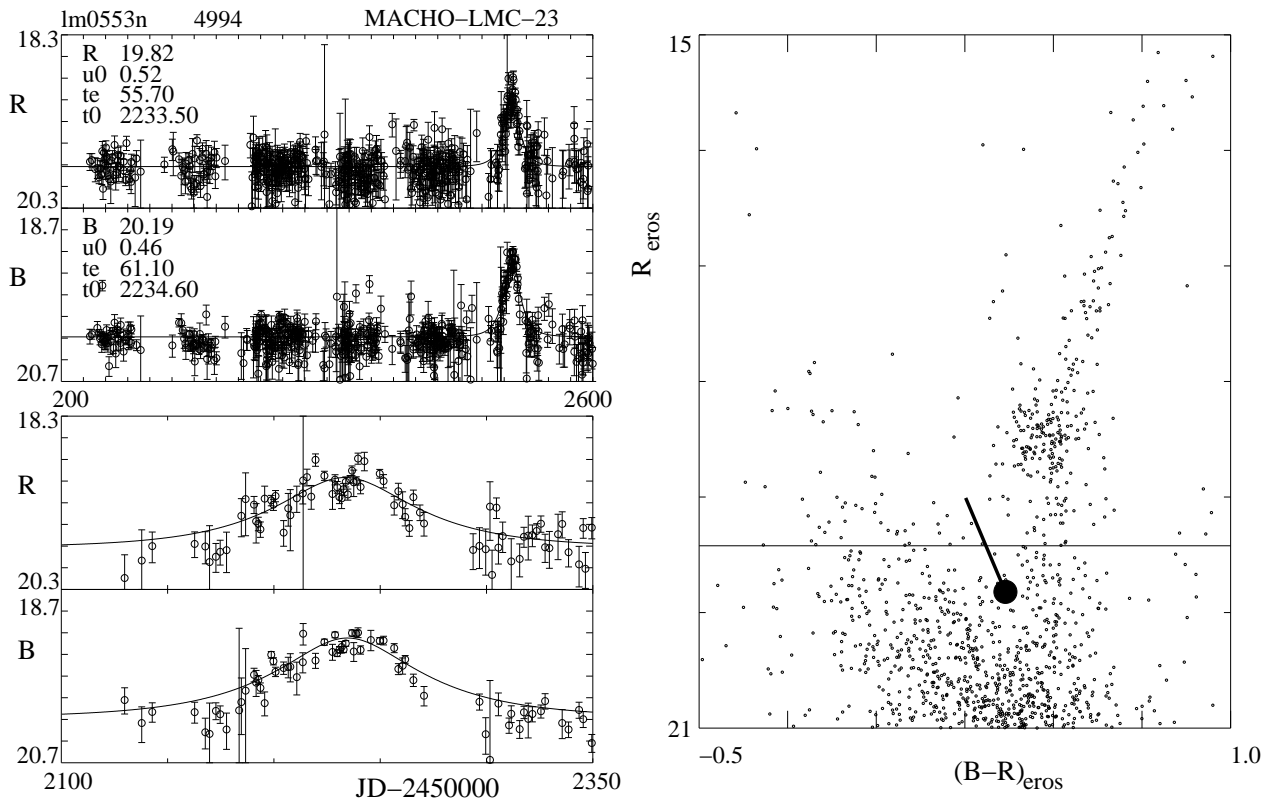


Fig. 10. The EROS-2 light curve of MACHO microlensing candidate MACHO-LMC-23. The curve shows a second variation, 6.8 years after the variation seen by MACHO. Also shown is the color-magnitude diagram of the star’s CCD-quadrant and the excursion of the event.

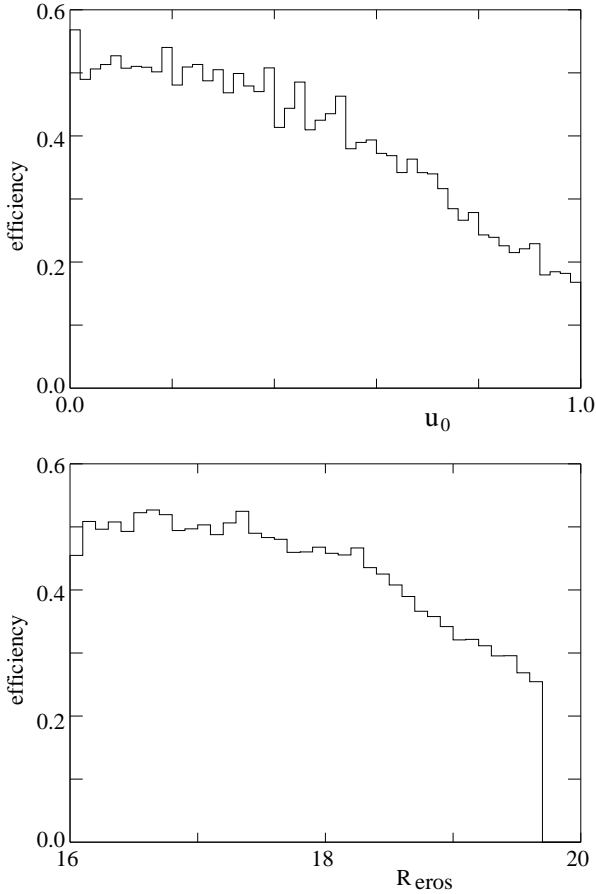


Fig. 13. The detection efficiency for simple microlensing light curves (10) as a function of u_0 (top) and of R_{eros} (bottom) for LMC and SMC events in the range $10 \text{ d} < t_E < 200 \text{ d}$.

t_E of interest for this work, the efficiency varies from ~ 0.25 at $t_E = 10 \text{ d}$ to ~ 0.45 at $t_E = 200 \text{ d}$.

Blended events have an efficiency that is reduced because an impact parameter smaller than unity is necessary to produce an amplification of 1.34. The efficiency is also modified because the time scale is reduced. To sufficiently good approximation we find

$$\epsilon_{ij}(\alpha_i, t_E) \sim \frac{u_i(2.18, \alpha_i)}{0.5} \epsilon(\alpha = 1, u_i(1, \alpha_i)t_E) \quad (14)$$

where $u_i(A_{\text{max}}, \alpha_i)$ is the impact parameter necessary to produce a maximum amplification A_{max} .

To evaluate the summed detection efficiency for a realistic distribution of α_1 and α_2 we used the pairs from the artificial images of Section 3, Figure 4. Figure 12 shows the ratio between the calculated sum (for the four studied fields) and the unblended efficiency. For $t_E = 40 \text{ d}$ the efficiency is reduced by a factor ranging from 0.90 in the sparse fields lm048 and lm034 to 0.92 and 0.97 in the denser fields lm019 and lm009. The brightest star, $i = 1$ accounts for 95% of the rate in the sparse fields and 88% in the dense fields.

Figure 13 shows the efficiency for unblended events as a function of u_0 and of R_{eros} for events with $10 \text{ d} < t_E < 200 \text{ d}$. The efficiency for the Bright-Star Sample has a much weaker dependence on u_0 and R_{eros} than that for the Full Sample. For the Full Sample the efficiency falls rapidly with increasing u_0 and R_{eros} (Tisserand 2004).

The efficiencies in Figures 11 and 13 are for the detection of microlensing events due to simple lenses. Events due to binary

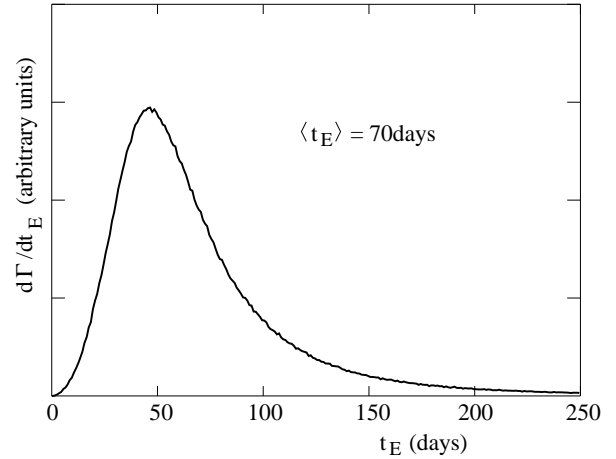


Fig. 14. The t_E distribution $d\Gamma/dt_E$ expected for $1M_{\odot}$ lenses in a spherically symmetric isothermal halo with core radius 5kpc, i.e. the S model used by the MACHO collaboration (Alcock et al. 2000b).

lenses with caustic crossings are discriminated against, mostly by C9. Of the 17 LMC events of the MACHO collaboration (Alcock et al. 2000b) only 1 event, MACHO-LMC-9, is of this type and would not pass our selection criteria. This event corresponds to $\sim 10\%$ of their optical depth. We note also that toward the Galactic Bulge $\sim 10\%$ of the observed microlensing events are due to binary lenses (Udalski et al. 2000a). To compensate for this loss of efficiency, we conservatively reduce the efficiency of Figure 11 by a factor 0.9 when calculating limits on the optical depth.

8. Limits on the abundance of machos

The microlensing optical depth, τ , is defined as the probability that any given star, at a given time, is amplified by at least 1.34, i.e. with an impact parameter $u < 1$. From a set of N_{ev} events, τ can be estimated from

$$\tau = \frac{\pi N_{\text{ev}}}{2N_{\text{stars}}T_{\text{obs}}} \left\langle \frac{t_E}{\epsilon} \right\rangle, \quad (15)$$

where $\langle t_E/\epsilon \rangle$ is the mean t_E divided by efficiency for the observed events.

In the LMC we have found no events so we can only give an upper limit on τ by calculating the expected number of events as a function of τ as given by (9). For this analysis we use the t_E distribution of the S model (Alcock et al. 2000b) shown in Figure 14. It relates $\langle t_E \rangle$ to the macho mass (assumed unique): $\langle t_E \rangle = 70 \text{ d} \sqrt{M/M_{\odot}}$. Limits using other halo models or macho mass distributions can be found to often good approximation by simply scaling (9) with $\epsilon(\langle t_E \rangle)/\langle t_E \rangle$.

The expected number of LMC events for $\tau_{\text{lmc}} = 4.7 \times 10^{-7}$ as a function of lens mass, M , is shown in Figure 15a. For $M = 0.4M_{\odot}$, we have $\langle t_E \rangle = 44 \text{ d}$, $\langle \epsilon \rangle = 0.35$, $N_{\text{star}} = 5.5 \times 10^6$ and $T_{\text{obs}} = 2500 \text{ d}$, giving 32 LMC events for EROS-2. We add 7 LMC events for EROS-1 to give a total of 39 expected events for $\tau_{\text{lmc}} = 4.7 \times 10^{-7}$.

For no observed events ($N < 3.0$, 95% CL), the 95% CL upper limit on the optical depth is

$$\frac{\tau}{4.7 \times 10^{-7}} < \frac{3}{N_{\text{ex}}(4.7 \times 10^{-7})} \quad (16)$$

For 39 expected events, The upper limit is then $\tau_{lmc} < 0.36 \times 10^{-7}$. The limit on τ_{lmc} as a function of M is shown in Figure 15b. In the t_E range favored by the MACHO collaboration, we find

$$\tau_{lmc} < 0.36 \times 10^{-7} \times [1 + \log(M/0.4M_\odot)] \quad 95\%CL, \quad (17)$$

i.e.

$$f < 0.077 \times [1 + \log(M/0.4M_\odot)] \quad 95\%CL, \quad (18)$$

where $f \equiv \tau_{lmc}/4.7 \times 10^{-7}$ is the halo mass fraction within the framework of the S model. This limit on the optical depth is significantly below the value for the central region of the LMC measured by the MACHO collaboration (Alcock et al. 2000b), $\tau_{lmc}/10^{-7} = 1.2^{+0.4}_{-0.3}(stat.) \pm 0.36(sys.)$ and the revised value of Bennett (2005), $\tau_{lmc}/10^{-7} = 1.0 \pm 0.3$. The Alcock et al. (2000b) optical depth used for the entire LMC predicts that EROS would see ~ 9 LMC events whereas none are seen.

For the SMC, the one observed event corresponds to an optical depth of 1.7×10^{-7} ($N_{star} = 0.86 \times 10^6$). Taking into account only Poisson statistics on one event, $0.05 < N_{obs} < 4.74$ (90% CL) this gives

$$0.085 \times 10^{-7} < \tau_{smc} < 8.0 \times 10^{-7} \quad 90\%CL. \quad (19)$$

This is consistent with the expectations of lensing by objects in the SMC itself, $\tau_{smc} \sim 0.4 \times 10^{-7}$ (Graff & Gardiner 1999). The value of $t_E = 125$ d is also consistent with expectations for self-lensing $\langle t_E \rangle \sim 100$ d for a mean lens mass of $0.35M_\odot$.

We also note that the self-lensing interpretation is favored from the absence of an indication of parallax in the light curve (Assef et al. 2006).

We can combine the LMC data and the SMC data to give a limit on the halo contribution to the optical depth by supposing that the SMC optical depth is the sum of a halo contribution, $\tau_{smc-halo} = \alpha\tau_{lmc}$ ($\alpha \sim 1.4$) and a self-lensing contribution τ_{sl} . (We conservatively ignore contributions from LMC self-lensing and from lensing by stars in the disk of the Milky Way.) For one observed SMC event with $t_E = 125$ d and zero observed LMC events, the likelihood function is

$$L(\tau_{lmc}, \tau_{sl}) \propto [\alpha\tau_{lmc}\Gamma'_h(t_E) + \tau_{sl}\Gamma'_{sl}(t_E)] \exp[-N(\tau_{lmc}, \tau_{sl})]$$

where $N(\tau_{lmc}, \tau_{sl})$ is the total number of expected events (LMC and SMC) as a function of the two optical depths as calculated with equation (8). The function $\Gamma'_h(t_E)$ is the distribution (normalized to unit integral) expected for halo lenses of mass M (Figure 14) and $\Gamma'_{sl}(t_E)$ is the expected distribution for SMC self-lensing taken from Graff & Gardiner (1999). We assume the SMC self-lensing optical depth is that calculated by Graff & Gardiner (1999) though the results are not sensitive to this assumption. For macho masses less than $1M_\odot$, the likelihood function is maximized for $\tau_{lmc} = 0$ because there are no LMC events in spite of the greater number of LMC source stars. For $M < 0.1M_\odot$ the limit on the halo contribution approaches that one would calculate for no candidates in either the LMC or the SMC because the observed t_E of 125 d is too long for a halo event. The calculated upper limit is shown as the dashed line in Figure 15b. In the mass range favored by the MACHO collaboration, the limit is slightly lower than that using only the LMC data. The combined limit would be somewhat stronger if we assumed an oblate halo ($\alpha < 1.4$) and somewhat weaker if we assumed a prolate halo ($\alpha > 1.4$). Constraints on the shape of the Milky Way halo were recently summarized by Fellhauer et al. (2006) who argued that the observed bifurcation

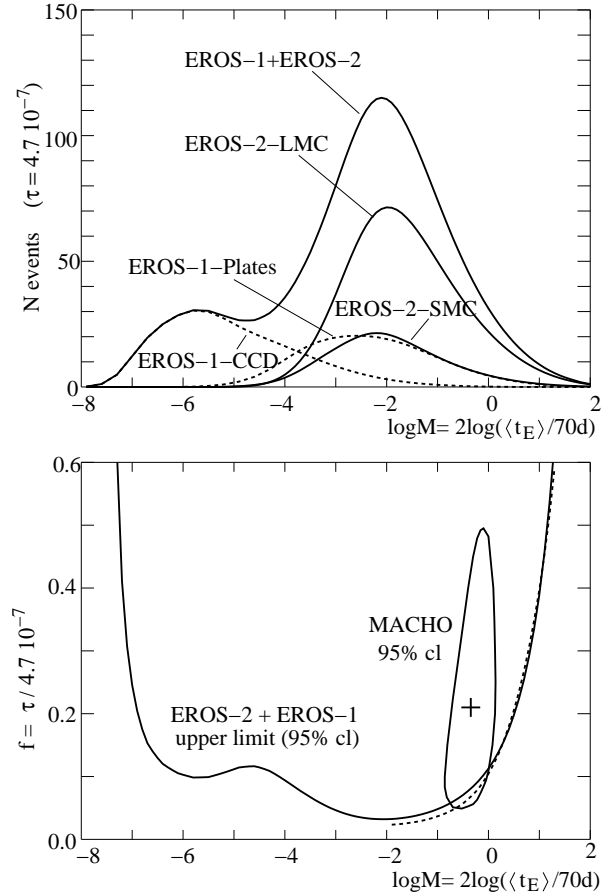


Fig. 15. The top panel shows the numbers of expected events as a function of macho mass M for the S model of Alcock et al. (2000b). The expectations for EROS-2-LMC, SMC (this work) are shown along with those of EROS-1 (Renault et al. 1997) with contributions from the photographic plate program (Ansari et al. 1996a) and CCD program (Renault et al. 1998). The number of events for EROS-2-SMC supposes $\tau_{smc} = 1.4\tau_{lmc}$. In the lower panel the solid line shows the EROS 95% CL upper limit on $f = \tau_{lmc}/4.7 \times 10^{-7}$ based on no observed events in the EROS-2 LMC data and the EROS-1 data. The dashed line shows the EROS upper limit on τ_{lmc} based on one observed SMC event in all EROS-2 and EROS-1 data assuming $\tau_{smc-halo} = 1.4\tau_{lmc}$. The MACHO 95% CL. curve is taken from Figure 12 (A, no lmc halo) of Alcock et al. (2000b).

of the Sagittarius Stream can be explained if the halo is close to spherical.

A possible systematic error in our result could come from our assumption that the optical depth due to binary lenses is small, 10% of the total. An alternative strategy would have been to relax the cuts so as to include the event shown in Figure 8. We have chosen not to do this because the light curve itself is not sufficiently well sampled to establish the nature of the event (other than that it is not a simple microlensing event) and also because of its anomalous position in the color-magnitude diagram. We note also that the optical depth associated with the event, $\tau = 0.7 \times 10^{-8}$, is a factor ~ 4 below the upper limit (17).

Another important question concerns the influence on our results of the Bright-Sample magnitude cut. Since the cut was not established before the event search, it is natural to ask if the position of the cut was chosen to give a strong limit. In fact, elimination of the cut would not change significantly the conclu-

sions of this paper. Four additional events (EROS2-LMC-8, 9, 10 and 11 from Table 2) were found with the analysis described in Appendix A. The baselines of the source stars of these events are on average 0.9 magnitude below the Bright Sample cut. An additional event (EROS2-LMC-12) with no R_{eros} data during the variation was found. The values of t_E for these events are in the range 10-60 days, similar to those in the MACHO sample. The optical depth associated with the four events seen in two colors is $(1.7 \pm 0.6) \times 10^{-8}$ (Tisserand 2004), not in contradiction with the limit from the Bright-Sample analysis. The 95% CL limit on the halo fraction is 12% at $M = 0.4M_{\odot}$. We prefer to use the limit from the Bright Sample for the reasons already mentioned: better understanding of blending and a superior photometry allowing better rejection of variable stars. Indeed, inspection of the light curves of EROS2-LMC-8-12 in Figures A.1-A.5 indicates that most are not especially convincing candidates. An exception is EROS2-LMC-8 but its position in the color-magnitude diagram and strongly chromatic magnification indicate that the event is most likely due to a lens in the Milky Way disk.

9. Discussion of the results

The limits shown in Figure 15 rule out machos as the majority of Galactic dark matter over the range $0.6 \times 10^{-7}M_{\odot} < M < 15M_{\odot}$. The limits are $f < 0.04$ for $10^{-3}M_{\odot} < M < 10^{-1}M_{\odot}$ and $f < 0.1$ for $10^{-6}M_{\odot} < M < 1M_{\odot}$. We note that even stronger limits in the range $10^{-7}M_{\odot} < M < 10^{-3}M_{\odot}$ were found (Alcock et al. 1998) by combining the data from the EROS-1 CCD program with those of the MACHO program. These data gave $f < 0.07$ for $M \sim 3 \times 10^{-6}M_{\odot}$. It should also be possible to improve limits in the range $10M_{\odot} < M < 100M_{\odot}$ by combining the results presented here with the MACHO high mass results (Alcock et al. 2001b). This may narrow the small remaining allowed macho mass range between the range excluded by microlensing and that excluded by the abundance of halo wide binary stars (Yoo, Chanamé and Gould 2004).

Initially, the EROS and MACHO programs were primarily motivated by the search for halo brown dwarfs of mass $0.02 - 0.08M_{\odot}$. Such objects are clearly ruled out as primary components of the Milky Way halo by Figure 15 (implying $f < 0.04$) and the data of the MACHO collaboration (Alcock et al. 2000b).

The observation of 17 events by MACHO with $\langle t_E \rangle \sim 40$ d suggested the existence of machos of $M \sim 0.4M_{\odot}$. Such objects could be invisible (e.g. primordial black holes) or faint (e.g. cool white dwarfs). However, the latter are not seen at the corresponding level in multi-color surveys (Gates et al. 2004) and high proper-motion surveys (Goldman et al. 2002; Reid 2005, and references therein).

At any rate, the EROS limit (17) is significantly less than the MACHO result $\tau_{\text{lmc}} = 1.2_{-0.3}^{+0.4} \times 10^{-7}$. However, there are considerable differences between the EROS and MACHO data sets that may help to resolve the conflict. Generally speaking, MACHO uses faint stars in dense fields (1.1×10^7 stars over 13.4 deg^2) while EROS-2 uses bright stars in sparse fields (0.7×10^7 stars over 84 deg^2). Of these bright EROS-2 stars, 0.2×10^7 are in MACHO fields.

The use of dense fields by the MACHO group suggests that the higher MACHO optical depth may be due, in part, to self-lensing in the inner parts of the LMC. This would contradict LMC models (Mancini et al. 2004) which suggest that only 1-3 MACHO events should be expected to be due to self-lensing. In fact, MACHO-LMC-14 is known to be due to self-lensing (Alcock et al. 2001c) because it has a binary source and the form

of the accompanying deformation of the lightcurve with respect to the simple microlensing lightcurve requires that the lens be in the LMC. A second event, MACHO-LMC-9, is due to a binary lens and the self-lensing interpretation can be avoided only by assuming that the source is also a binary system and that each of the two widely separated components happened to land on the caustic on the two successive observations made of the caustic entrance (Alcock et al. 2000a).

If it turns out that the self-lensing rate is higher than the model estimates in the MACHO fields but still negligible in the outer fields of the LMC, the disagreement between MACHO and this work is considerably reduced. Since only 1/3 of our Bright Sample stars are in MACHO fields, the EROS-2 95% CL upper limit on τ for the MACHO fields is the limit (17) multiplied by a factor 3, consistent with the Alcock et al. (2000b) result as modified by Bennett (2005).

A possible explanation for the discrepancy that is similar to self-lensing is the possibility that the events are due to halo lenses but the Halo is clumpy and that the MACHO-fields lie behind a clump of size less than that of the EROS-2 fields. The effect of a clumpy halo on the optical depth was discussed by Holopainen et al. (2006) though they did not discuss directly the possibility that it could resolve the EROS-MACHO controversy. At any rate, if this is the cause of the discrepancy, the EROS-2 result gives the more representative optical depth because it is based on a larger solid angle.

The use of faint stars by MACHO may also give an explanation of the disagreement. Only two of the 17 MACHO candidates (MACHO-LMC-18 and 25) are sufficiently bright to be in our Bright-Star Sample. Of these two, MACHO-LMC-18 is in the EROS Bright-Sample only because the EROS starfinder mixed two similar objects that are resolved by the MACHO starfinder.

The use of faint stars by MACHO suggests two possible explanations for the disagreement. The first would be contamination by variable stars that, in our Bright-Star Sample, are either not present or identified as such because of superior photometric precision. The low photometric precision for the faint LMC stars makes most of the events less convincing than the events on bright stars in the Galactic Bulge or the one EROS event in the SMC. Indeed, one of the MACHO A events, MACHO-LMC-23, has been identified as a variable star by a second variation in the EROS-2 data shown in Figure 10 (Tisserand 2004). As already noted, Bennett et al. (2005) argued that MACHO-LMC-23 was, in any case, a weak candidate and that its variability doesn't call into question the nature of the other MACHO candidates. Indeed, some of the MACHO candidates are very convincing microlensing candidates. In particular, MACHO-LMC 1, 5, 9, 14 and 21 are strong candidates based only on MACHO photometry while Bennett et al. (2005) argued that MACHO-LMC-4, 13 and 15 are strong candidates because of high precision followup photometry. We might note, however, that of these candidates, MACHO-LMC-14 is most likely due to LMC self-lensing and MACHO-LMC-5 is due to lensing by a normal red-dwarf star in the disk of the Milky Way (Alcock et al. 2001d; Gould 2004).

The second possible explanation related to the use of faint source stars is the large blending effects that must be understood. Alcock et al. (2000b, 2001a) suggest a 30% systematic error to reflect this uncertainty. The experience with the use of faint stars in the Galactic Bulge suggests that this uncertainty may be underestimated, though in principle the star distribution is better understood in the LMC than in the Bulge. At any rate, the extension of the limits presented here, either by EROS or by OGLE-3 or SuperMACHO, will require the use of faint stars and a good understanding of blending.

Acknowledgements. Over the last 17 years, the EROS collaboration has profited from discussions with members of the MACHO collaboration, especially Charles Alcock (who introduced us to machos and microlensing), Dave Bennett, Kim Griest and Chris Stubbs. We thank Annie Robin for help with the Galactic model calculations. We are grateful to the technical staff of ESO, La Silla for the support given to the EROS-2 project. We thank J-F. Lecoine and A. Gomes for the assistance with the online computing and the staff of the CC-IN2P3, especially the team in charge of the HPSS storage system, for their help with the data management. AG was supported by grant AST-0452758 from the NSF and JA by the Danish Natural Science Research Council. Finally, we thank the referee for questions and comments that led to significant improvements in this paper.

Appendix A: Candidate selection for the full sample

In this paper we have concentrated on the analysis of the Bright-Star Sample of stars because this leads to the most reliable limits of the optical depth. A search for microlensing events on the full sample of stars was also performed (Tisserand 2004). The candidates found in this search are listed in Table 2 and displayed in Figures A.1-A.5. In this section we list the selection criteria leading to this set of candidates.

The criteria are very similar to those described in Section 4 for the Bright-Star Sample. However, the problems encountered with analyzing low precision light curves necessarily led to more complicated criteria to avoid the many spurious events caused by photometric problems. In all, 17 criteria, $c1 - c17$, were applied compared to the 12 criteria, $C1 - C12$, applied to the Bright-Star Sample.

The first four criteria are identical to those applied to the Bright-Star Sample:

$$c1 = C1 \quad c2 = C2 \quad c3 = C3 \quad c4 = C4 .$$

We then required that the total amplitude of luminosity variation along the light curve be greater than 5 times the point-to-point dispersion, σ_{base} in the light curve, recomputed after excluding the most significant excursions:

$$c5 : \quad F_{5max} - F_{5min} > 5\sigma_{base} .$$

Here F_{5max} and F_{5min} are the maximum and minimum fluxes averaged over any 5 neighboring measurements.

For excursions with a regular variation, the point-to-point dispersion of the measured fluxes within the excursion, $\sigma_{ptp,exc}$, obtained from the comparison of each measured flux with the linear interpolation of its two neighbors (in time), is normally smaller than the global dispersion, σ_{exc} , i.e. the width of the distribution of all fluxes within the excursion. To exclude irregular variations, we require that their ratio be sufficiently small;

$$c6 : \quad \frac{\sigma_{ptp,exc}}{\sigma_{exc}} < 0.90 .$$

Cuts $c4 - c6$ are applied independently in the two passbands. Light curves are retained if they are selected in one passband at least. This reduces the star sample to slightly less than 0.1% (28,500 objects) of the full sample.

The next two criteria are similar to $C5$ and $C9$ applied to the Bright-Star Sample

$$c7 : \quad \left[\frac{\chi^2 - N_{dof}}{\sqrt{2N_{dof}}} \right]_{base} < 15 ,$$

$$c8 : \quad \left[\frac{\chi^2 - N_{dof}}{\sqrt{2N_{dof}}} \right]_{peak} < 10 .$$

The next cut, $c9$, deals with a background connected to the realignment of the telescope optics in May 1998, which slightly

changed the PSF. Faint stars near a diffraction feature in the PSF of bright stars were affected; this was seen as light curves with two plateaus, one (higher) before and one (lower) after May 1998. A rather complicated algorithm was developed to identify such light curves. It relies mostly on the relative flux values of the two stars, their distance and the relative height of the two plateaus in the light curve. The details can be found in (Tisserand 2004) but we note that it affects our efficiency only for $t_E > 150$ d.

$c9$: no influence of telescope realignment

At this point we accepted only light curves that passed criteria $c1 - c9$ in both colors:

$c10$: $c1 - c9$ red and blue

Criterion $c11$ is similar to $C7$:

$c11$: $N_{peak} > 4$; ≥ 2 points in rise ; ≥ 2 points in fall .

The remaining cuts follow closely the cuts for the Bright-Star Sample

$c12 = C6$

$c13$: $u_{0r} < 1$ or $u_{0b} < 1$

$c14$: $\frac{\chi_{ct}^2 - \chi_{ml}^2}{\chi_{ml}^2 / N_{dof}} \frac{1}{\sqrt{2N_{dof,peak}}} > 50$ in R or B .

Criterion $c15$ eliminates light echos from SN1987a by requiring

$c15$: Distance event - SN1987a > 30 arcmin .

Finally, $c16$ and $c17$ are the blue bumper and supernovae criteria $C10$ and $C11$ supplemented by a visual rejection of events superimposed on background galaxies.

The first six events in Table 2 passed the cuts $c1-c17$. A monochromatic analysis was performed where $c10$ was removed and candidates were only required to pass the other criteria in either of the two colors. About 500 events were scanned by eye. Only one event, EROS2-LMC-12, was found, the others being due to photometric problems or long period variable stars.

References

- Afonso, C., Albert, J. N., Alard, C. et al. (EROS-2 coll.), 1998, A&A, 337, L17
Afonso, C., Alard, C., Albert, J.N. et al. (EROS-2 coll.), 1999, A&A, 344, L63
Afonso C., Alard, C., Albert, J.N. et al. (EROS-2 , MACHO -GMAN , MPS , OGLE and PLANET colls.), 2000, ApJ, 532, 340
Afonso, C., Albert, J. N., Andersen, J., et al. (EROS-2 coll.) 2003a, A&A, 400, 951
Afonso, Albert, J. N., Alard, C., et al. (EROS-2 coll.) 2003b, A&A, 404, 145
Alcock, C. Allsman, R.A., Alves, D. et al. (MACHO coll.), 1997a, ApJ, 486, 697
Alcock, C. Allsman, R.A., Alves, D. et al. (MACHO coll.), 1997b, ApJ, 491, L11
Alcock, C. Allsman, R.A., Alves, D. et al. (MACHO and EROS-1 colls.), 1998, ApJ, 499, L9
Alcock, C., Allsman R. A., Alves D. R., et al. (MACHO coll.) 2000a, ApJ, 541, 270
Alcock, C., Allsman, R. A., Alves, D. R., et al. (MACHO coll.) 2000b, ApJ, 542, 281
Alcock, C., Allsman, R. A., Alves, D. R., et al. (MACHO coll.) 2001a, ApJS, 136, 439
Alcock, C., Allsman, R. A., Alves, D. R., et al. (MACHO coll.) 2001b, ApJ, 550, L169
Alcock, C., Allsman, R. A., Alves, D. R., et al. (MACHO coll.) 2001c, ApJ, 552, 259
Alcock, C., Allsman, R. A., Alves, D. R., et al. (MACHO coll.) 2001d, Nature, 414, 617

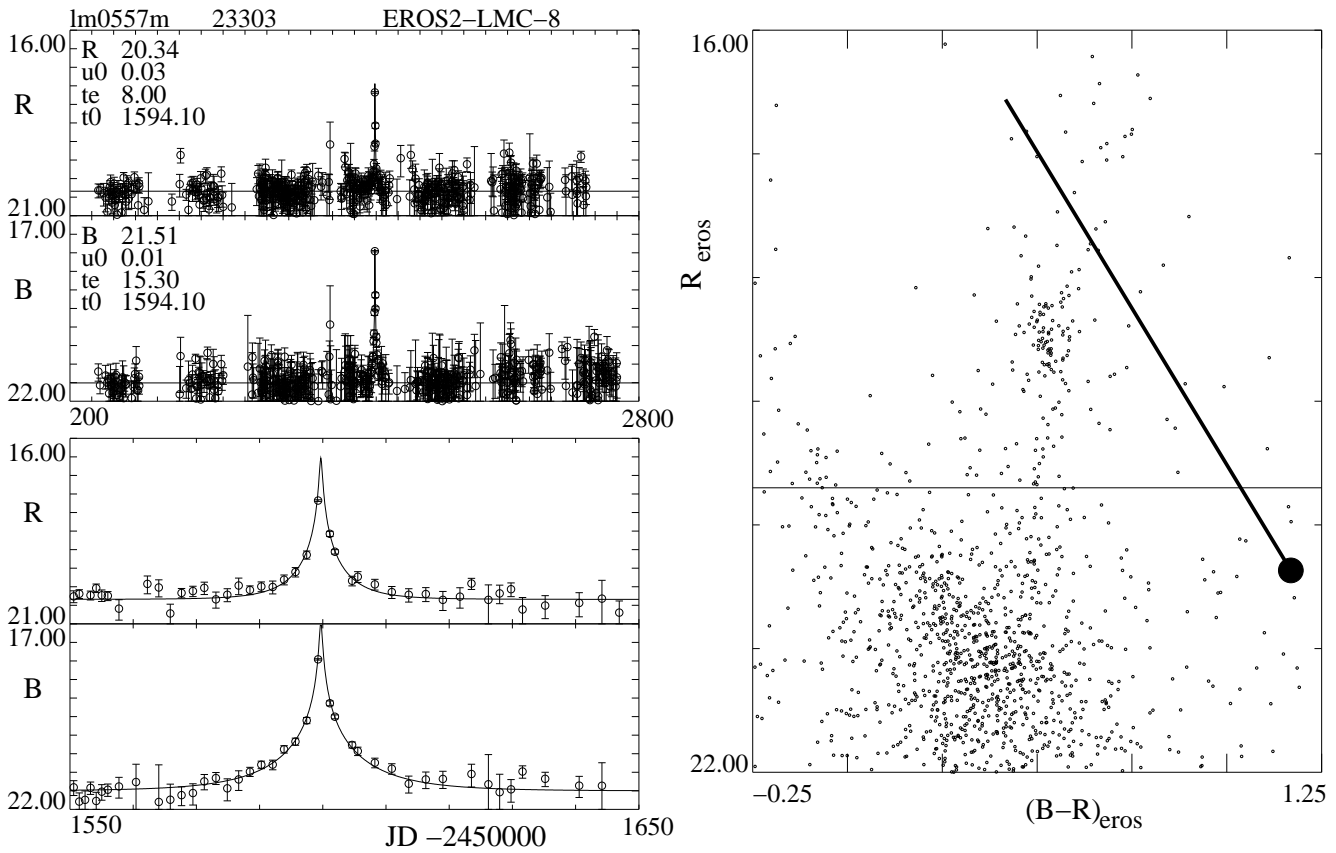


Fig. A.1. The light curves of EROS-2 star Im055-7m-23303. Also shown is the color-magnitude diagram of the star's CCD-quadrant and the excursion of the event.

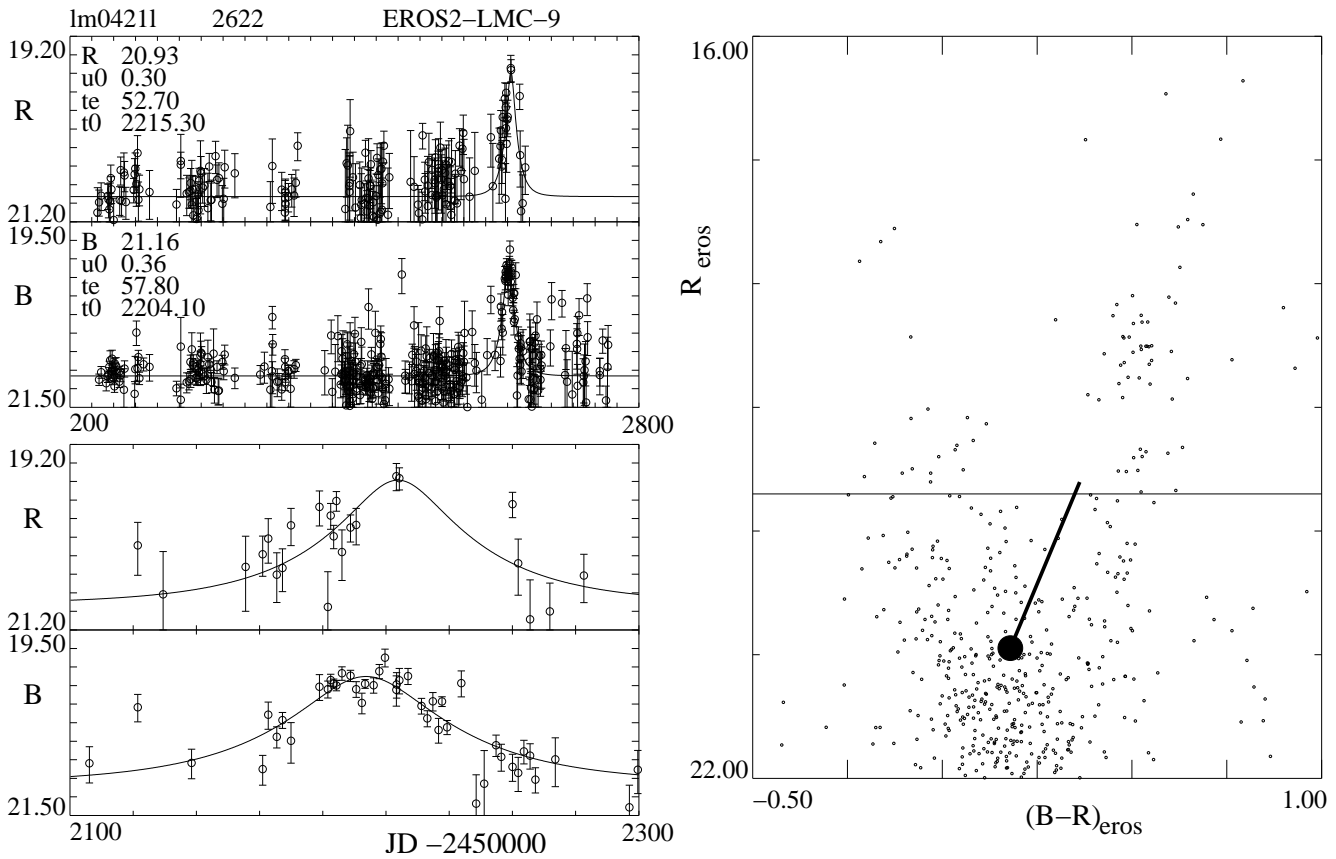


Fig. A.2. The light curves of EROS-2 star Im042-11-2622. Also shown is the color-magnitude diagram of the star's CCD-quadrant and the excursion of the event.

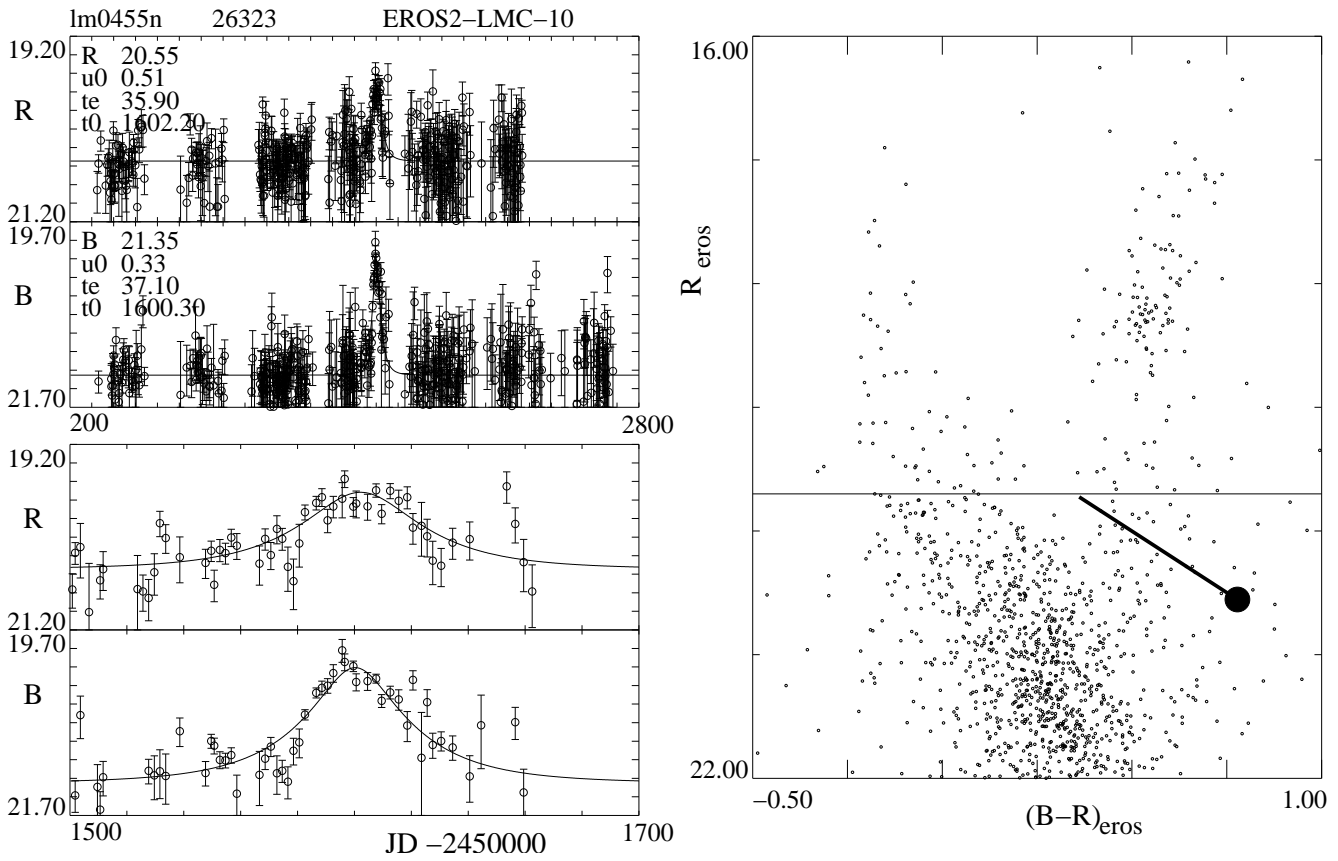


Fig. A.3. The light curves of EROS-2 star lm045-5n-26323. Also shown is the color-magnitude diagram of the star's CCD-quadrant and the excursion of the event. Note the visible asymmetry in the B light curve, possibly indicative of a supernova.

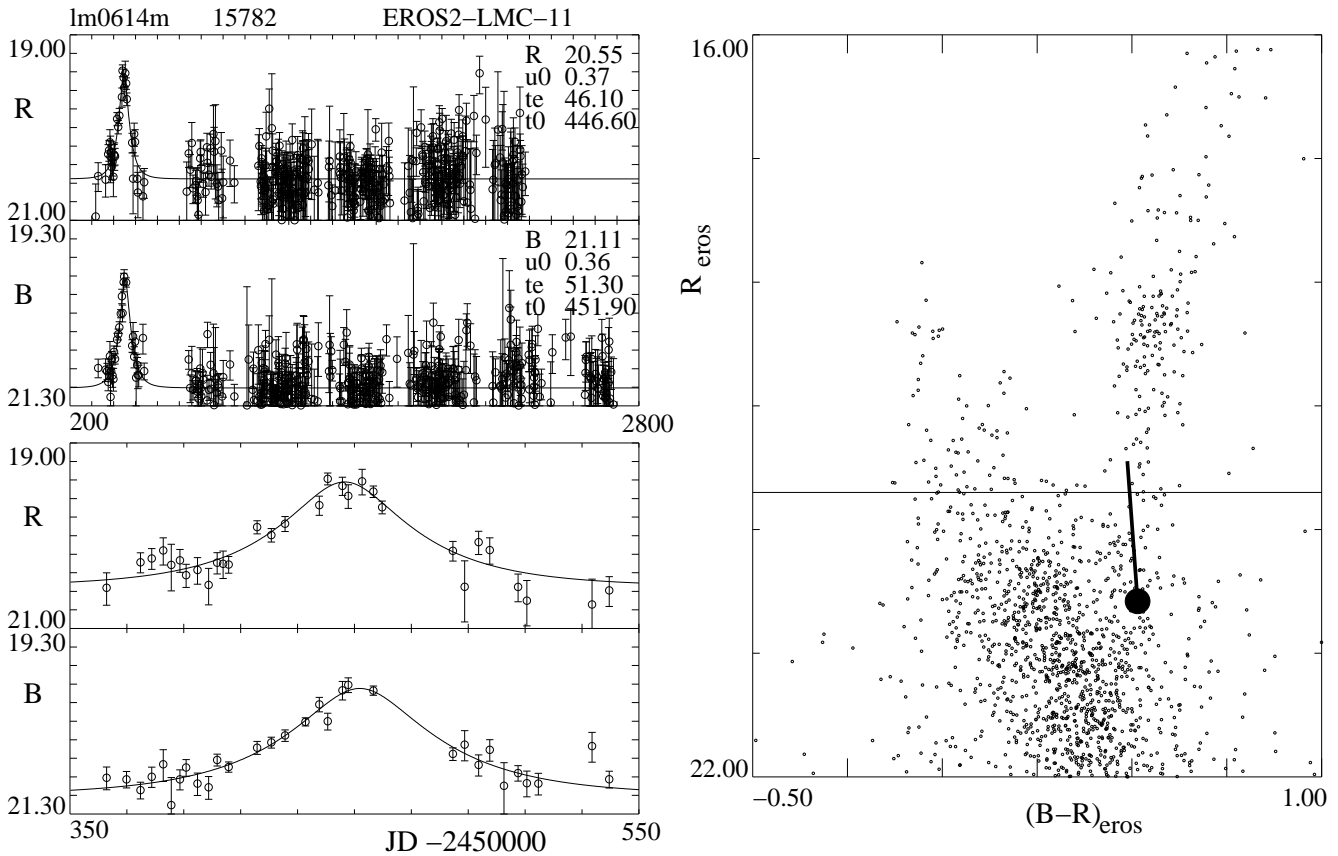


Fig. A.4. The light curves of EROS-2 star lm061-4m-15782. Also shown is the color-magnitude diagram of the star's CCD-quadrant and the excursion of the event.

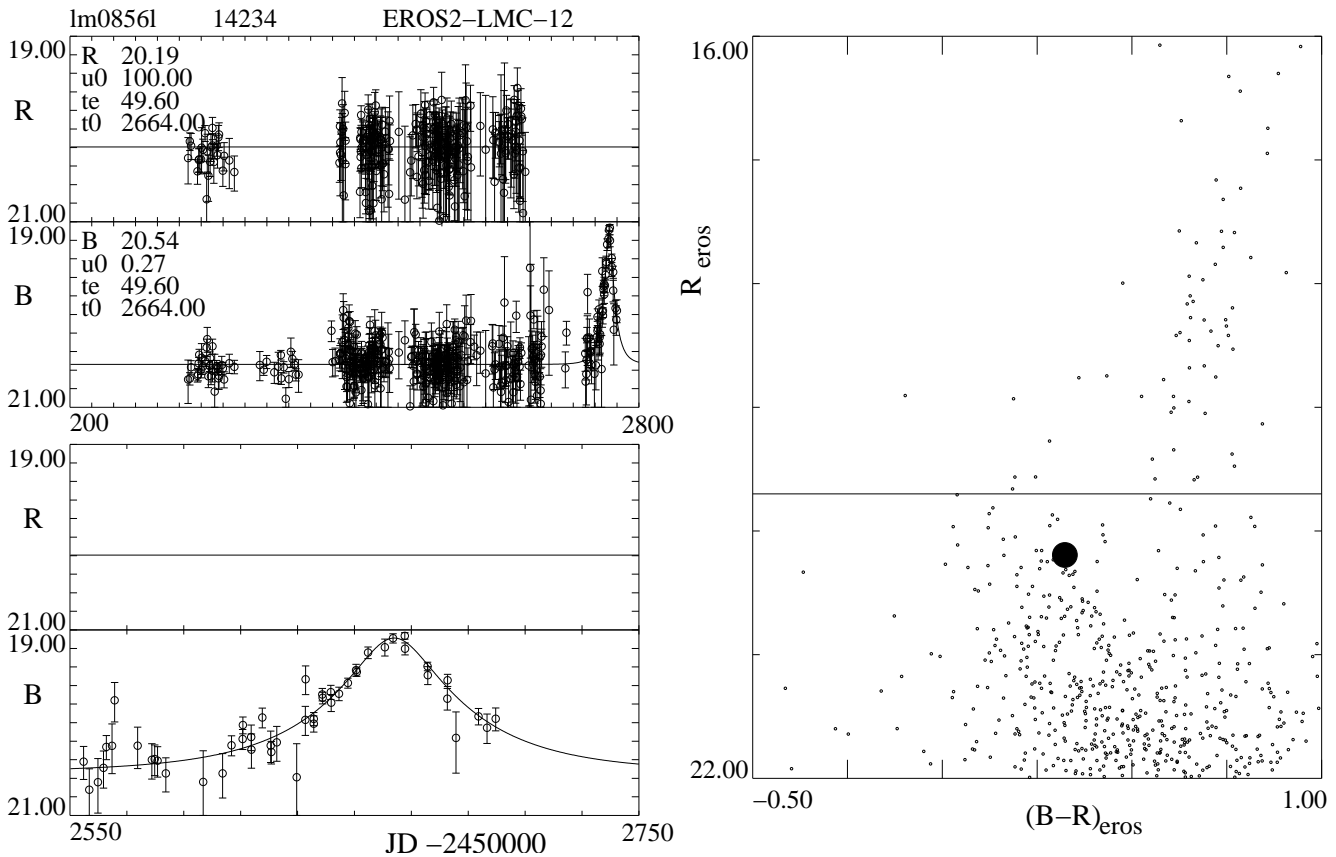


Fig. A.5. The light curves of EROS-2 star lm085-6l-14234. Also shown is the color-magnitude diagram of the star's CCD-quadrant and the position of the source's baseline.

- Ansari, R., Cavalier, F., Moniez, M., et al. (EROS-1 coll.) 1996a, *A&A*, 314, 94
 Ansari, R. et al. (EROS-2 coll.) 1996b, *Vistas in Astronomy*, 40, 519
 Assef, R.J., Gould, A., Afonso, C., et al 2006, *ApJ*, 649, 954
 Aubourg, É. et al., (EROS-1 coll.), 1993, *Nature*, 365, 623
 Bauer, F. et al. (EROS-2 coll.) 1997, Proceeding of the "Optical Detectors for Astronomy" workshop, ESO
 Beaulieu, J.-Ph., Ferlet, R., Grison, Ph. et al., (EROS-1 coll.), 1995, *A&A*, 299, 168
 Bennett, D. P., Becker, A. C., & Tomaney, A. 2005, *ApJ*, 631, 301
 Bennett, D. P. 2005, *ApJ*, 633, 906
 Bissantz, N. and Gerhard, O., 2002, *MNRAS*, 330, 591
 Bond, I.A., Rattenbury, N.J., Skuljan, J., et al. 2002, *MNRAS*, 333, 71-83.
 Calchi Novati, S., Paulin-Henriksson, S., An, J., et al. (AGAPE coll.) 2005, *A&A*, 443, 911
 de Jong, J. T. A., Widrow, L.M., Cseresnjejs, P., et al. (MEGA coll.) 2006, *A&A*, 446, 855
 Evans, N.W. & Belokurov, V. 2002, *ApJ*, 567, L119
 Fellhauer, M., Belokurov, V., Evans, N.W., et al. 2006, *ApJ*, 651, 167
 Gates, E., Gyuk, G., Harris, H. C., et al. (SDSS coll.) 2004, *ApJ*, 612, 132
 Goldman, B., Afonso, C., Alard, C., et al. (EROS-2 coll.) 2002, *A&A*, 389, 69
 Gould, A. 2004, *ApJ*, 606, 319
 Graff, D. & Gardiner, L.T. 1999, *MNRAS*, 307, 577
 Griest, K. 1991, *ApJ*, 366, 412
 Hamadache, C., Le Guillou, L., Tisserand, P., et al (EROS-2 coll.) 2006, *A&A*, 454, 185
 Han, C. and Gould, A. 2003, *ApJ*, 592, 172
 Holopainen, J., Flynn, C., Knebe, A., et al., 2006, *MNRAS*, 368, 1209
 Joshi, Y.C., Pandey, A.K., Narasimha, D. & Sagar, R. (Nainital coll.) 2005, *A&A*, 433, 787
 Lasserre, T. 2000, Thesis Université de Paris VI, <http://tel.ccsd.cnrs.fr/>
 Lasserre, T., Afonso, C., Albert, J.N. et al., (EROS-2 coll.), 2000, *A&A*, 355, L39
 Le Guillou, L. 2003, Thesis Université de Paris VI, <http://tel.ccsd.cnrs.fr/>
 Mancini, L., Calchi Novati, S., Jetzer, Ph., & Scarpetta, G. 2004, *A&A*, 427, 61
 Milsztajn, A. and Lasserre, T. (for the EROS-2 coll.), 2001, *Nucl. Phys. B (Proc. Suppl)* 91, 413
 Paczyński, B. 1986, *ApJ*, 304, 1
 Paczyński, B., 1996, *ARA&A*, 34, 419
 Palanque-Delabrouille, N., Afonso, C., Albert, J. N., et al. (EROS-2 coll.), 1998, *A&A*, 332, 1
 Petrou, M., 1981. Ph.D. thesis, University of Cambridge
 Popowski, P., Griest, K., Thomas, C. L., et al. (MACHO coll.) 2005, *ApJ*, 631, 879
 Reid, I.N. 2005, *ARA&A*, 43, 247
 Renault, C., Afonso, C., Aubourg, E., et al. (EROS-1 coll.) 1997, *A&A*, 324, L69
 Renault, C., Aubourg, E., Bareyre, P., et al. (EROS-1 coll.) 1998, *A&A*, 329, 522
 Riffeser, A., Fliri, J., Bender, R., et al. (WeCapp coll.) 2003, *ApJ*, 599, L17
 Robin, A., Reylé, C., Derrière, S., & Picaud, S. 2003, *A&A*, 409, 523; and 2004, *A&A*, 416, 157
 Sackett, P.D. and Gould, A., 1993, *ApJ*, 419, 648
 Sumi, T., Wozniak, P. R., Udalski, A., et al. (OGLE coll.) 2006, *ApJ*, 636, 240.
 Tisserand, P. 2004, Thesis Université de Nice, <http://tel.ccsd.cnrs.fr/>
 Udalski, A., Szymański, M., Kubiak, M., et al. (OGLE coll.), 1997, *Acta Astron.*, 47, 431
 Udalski A., Zebun K., Szymanski M., et al. (OGLE coll.) 2000a, *Acta Astron.*, 50, 1
 Udalski, A., Szymanski, M., Kubiak, M., et al. (OGLE coll.) 2000b, *Acta Astron.*, 50, 307
 Uglesich, R.R., Crotts, A. P. S., Baltz, E.A., et al. (VATT coll.) 2004, *ApJ*, 612, 877
 Wood, A. and Mao, S. 2005, *MNRAS*, 362, 945
 Yoo, J., Chanamé J., and Gould, A. 2004, *ApJ*, 601, 311
 Zaritsky Z., Harris J., Thompson I., and Grebel, E. 2004, *AJ*, 128, 1606